

Spectra from the shocked nebulae revealing turbulence near the Galactic Centre

M. Contini¹ and I. Goldman^{2*}

¹*School of Physics and Astronomy, Tel Aviv University, Tel Aviv 69978, Israel*

²*Afeka, Tel Aviv Academic College of Engineering, Tel Aviv 69107, Israel, email: goldman@afeka.ac.il*

Accepted: Received ; in original form 2010 month day

ABSTRACT

The spectra emitted from clouds near the Galactic Centre (GC) are investigated calculating the UV-optical-IR lines using the physical parameters and the element abundances obtained by the detailed modelling of mid-IR observations. The graphical presentation of the spectra reveals the strong lines. The characteristic line ratios calculated at the nebula provide information about the dereddened spectra emitted from regions near the GC. These line ratios are compared with those observed in active galaxies. We have found that the physical conditions in the nebulae near the GC are different from those of starburst galaxies and AGN, namely, gas velocities and densities as well as the photoionization fluxes are relatively low. The geometrical thickness of the emitting filaments is particularly small suggesting that matter is strongly fragmented by instabilities leading to an underlying shock-generated turbulence. This is revealed by the power spectra of the radial velocities, of the mid-IR continuum flux and of the computed Si/H relative abundances. Moreover, turbulence could amplify the initial magnetic fields.

Key words: Galaxy:centre–shock waves–radiation mechanisms–turbulence:general–ISM:abundances–galaxies:line spectra

1 INTRODUCTION

The Galaxy should be the largest information source about high and low-ionization level lines, however the central regions cannot be observed in the optical and UV range because of strong extinction (Schultheis et al. 2009).

Spectroscopic data in the infrared, UV, and in the X-ray range were lacking[†] before the Spitzer, FUSE, and XMM era, respectively. In recent years, Spitzer infrared spectra observed by Simpson et al (2007) and references therein and modelled in detail by Contini (2009, hereafter Paper I) allowed a detailed investigation of the gas and dust structures near the Galactic Centre (GC). The most serious problem was to obtain the spectra that had been properly corrected for extinction.

Fig. 1 (top) shows a radio image of this region (Yusef-Zadeh & Morris 1987). A sketch of the entire Galaxy (Nakanishi & Sofue 2006) is given in Fig. 1 (bottom) in order to emphasize the relatively small extent of the observed region.

The Sgr A West HII region contains a quiescent black hole $\sim 4 \cdot 10^6 M_{\odot}$ (Ghez et al. 2005; Eisenhauer et al. 2005) which is coincident with the radio source Sgr A* and is located at the GC. It also contains a cluster of massive stars. Two other clusters of young massive stars and massive molecular clouds (Schödel et al. 2006) appear in the GC, the Arches Cluster and the Quintuplet Cluster located ~ 25 pc away in the plane of the sky. The very massive Arches Cluster (Nagata et al 1995 and Cotera et al. 1996) of young stars heats and ionizes the region of the Arched Filaments and the Quintuplet Cluster ionizes the Sickle.

The star flux from the Quintuplet Cluster affects the clouds in the extended region including the Bubble. A detailed description of the GC is given by Simpson et al (2007).

The spectra were observed by Simpson et al. with the Spitzer IRS instrument, at 38 locations scanning across the Galactic plane; the locations and largest observed aperture size are presented in Fig. 1 (top). Accurate modelling and the precision of the data fit (Paper I) allowed evaluation of the physical conditions of the emitting gas, such as temperatures, densities, velocities, the magnetic field and the relative abundances of the elements. Moreover, the spectra contain a number of lines from different excitation levels

* Itzhak Goldman thanks the Department of Astronomy and Astrophysics, Tel Aviv University, for the hospitality while on Sabbatical Leave from Afeka College.

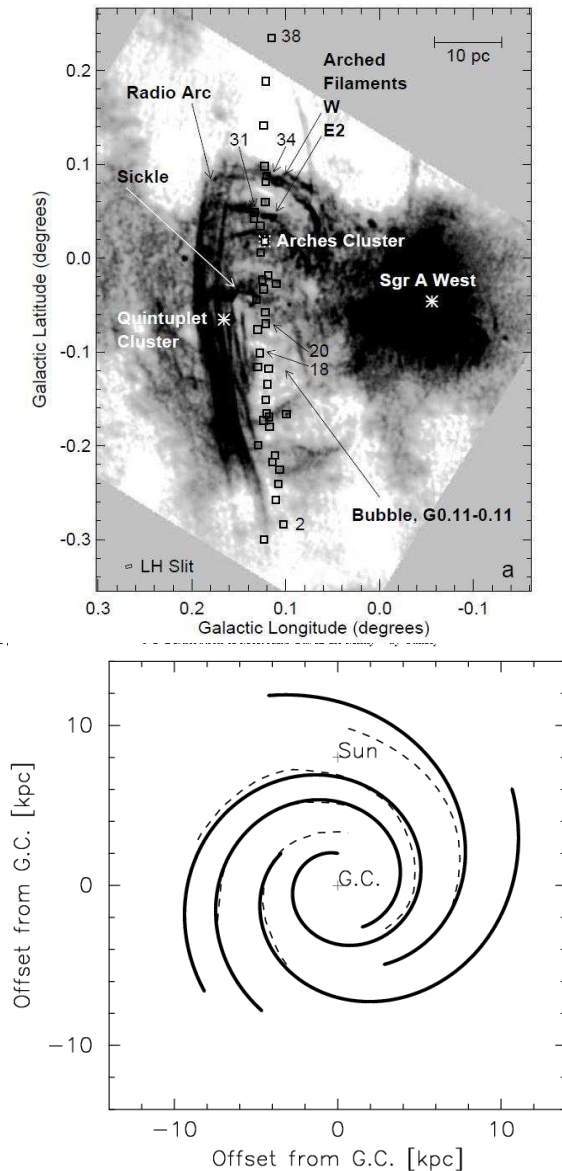


Figure 1. Top : Image of the Galactic Center with the observed positions as square boxes upon the radio continuum imaged at 21 cm by Yusef-Zadeh & Morris (1987) adapted from Simpson et al (2007, fig. 1). Bottom : The sketch of the Galaxy spiral arms is adapted from Nakanishi & Sofue (2006), fig. 15

and from different elements enough to constrain the models. This suggests that the same models which could reproduce the observational data in the IR could reproduce the data also in other ranges, e.g. optical, UV, etc.

So we present in Tables 1-4 model results for lines which were not included in Paper I. Most of the lines, particularly in the UV, cannot be observed because of extinction. Our aim is to provide a tool for correction once the spectra will be observed at least as upper limits.

We adopt a simple graphical method which shows predicted dereddened spectra and permits a rapid comparison with the spectra observed in other galaxies. The most significant lines throughout a large spectral range, from SiIII 1206 close to the Ly α line up to the FIR, [CII] 156 and [NII]

203, are selected. The UV-optical lines are in Å, while the IR lines are in μm throughout all the paper. The spectra are presented in Sect. 2.

We concluded in Paper I that the spectra observed in the nebulae near the GC show the characteristics of HII regions. However, an active nucleus, even if very weak is not excluded. So we will compare the mid-IR line ratios emitted from nebulae near the GC with those of LINERs, AGN, starburst galaxies, etc.

Some significant line ratios observed in the IR are analysed in Sect. 2.1 and 2.2. In the optical and UV ranges we will use model results which are constrained by the mid-IR observations. In Sects. 2.3 and 2.4 the line ratios calculated for nebulae near the GC are compared with the set of spectra observed at different positions throughout single galaxies and with the ensemble of line ratios observed from a sample of active galaxies (starbursts, AGN, etc.). The model calculations account for photoionization and for shocks. In Sect. 3 the results are discussed in the light of shock generated turbulence. Concluding remarks follow in Sect. 4.

2 THE LINE SPECTRA

The spectra are calculated adopting the code SUMA (see <http://wise-obs.tau.ac.il/~marcel/suma/index.htm> for a detailed description), that simulates the physical conditions of an emitting gaseous cloud under the coupled effect of photoionisation from an external radiation source and shocks. Both line and continuum emission from the gas are calculated consistently with dust reprocessed radiation, in a plane-parallel geometry.

The input parameters are: the shock velocity V_s , the preshock density n_0 , the preshock magnetic field B_0 , the colour temperature of the hot star T_* , the ionization parameter U for black body (BB) dominated fluxes, or the power-law (pl) flux reaching the nebulae from the active center F_h in number of photons $\text{cm}^{-2} \text{s}^{-1} \text{eV}^{-1}$ at the Lyman limit. The geometrical thickness of the emitting nebula D , the dust-to-gas ratio d/g , and the abundances of He, C, N, O, Ne, Mg, Si, S, A, Fe relative to H are also accounted for. Solar abundances are adopted (Allen 1976) in the models presented by Contini & Viegas (2001a,b). The distribution of the grain radius downstream is determined by sputtering, beginning with an initial radius of $0.2 \mu\text{m}$.

We refer to the regions observed in 38 positions near the GC by Simpson et al. (2007). The absolute intensities of the most important lines (Tables 1-4) emerging from a zero intensity continuum are shown in graphical form in Fig. 2. The spectra show the line intensities but they do not include the line profiles.

This representation is not aimed to measure or compare in detail the line intensities. That should be done using the Tables 1-4. We are interested in showing the trend, e.g. the rising and fading of some important lines close to the clusters and in the ISM. The spectra from the positions close to 17-25 show the photoionizing effect from the Quintuplet Cluster, while the filaments from positions close to 27-35 are photoionized by the Arches Cluster.

Notice that [NII] 203 appears in some intermediate positions (31-35, 10-13, 23-26), while [CII] 156 is always present, explaining its detection in many other galaxies.

Moreover, the UV and mid-IR lines are all of comparable strength. The spectra are very different from those of starburst galaxies (Fig. 4) calculated with higher V_s , and n_0 which are dominated by lines in the optical range. The spectra corresponding to LINER conditions are strong in the same ranges as those of the GC, but the line ratios are very different.

The graphical presentation allows for easy recognitions of the lines strong enough to be observed in the GC (IR spectra) and in other galaxies (UV-optical-IR spectra) and therefore useful for comparison purposes.

The corresponding models indicate the characteristic conditions of the emitting gas. The models adopted for the calculations which lead to the best fit of the mid-IR observations are given in Paper I (table 2 and fig 2).

The UV-optical lines appear in the left diagrams of Fig. 2, while the IR-FIR spectra are shown in the right diagrams. The line absolute fluxes calculated at the nebula cover a relatively large range in order to distinguish between strong and weak lines. The line intensities are given in $\log \nu F_\nu$ ($\text{erg cm}^{-2} \text{s}^{-1}$) spanning four orders on the Y-axis scale of the right diagram for each position. The spectra in Fig. 2 which refer to the observed positions (Fig. 1, top diagram) are labelled on the left of the diagrams. The spectra are constrained by the comparison of calculated (Contini 2009) with observed (Simpson et al 2007) line ratios in the mid-IR.

It can be noticed (Fig. 2, left diagram) in the regions near the GC that the $\text{Ly}\alpha$ and $\text{CIII}]$ 1909 lines are the strongest in the UV, while in the optical range $\text{[OII]} 3727$ and $\text{H}\alpha$ dominate near the Arches Cluster. The $\text{[NII]} 6583+6548$ and $\text{[SII]} 6717+6731$ lines can also be strong in some positions depending on the N/H and S/H relative abundances. In the IR range $\text{[SIII]} 33.5$ is generally the strongest line. The $\text{[CII]} 156$ line appears throughout most of the observed region. Lines are stronger in regions corresponding to higher densities (Paper I, fig. 2).

In Figs. 3 and 4 we present a small selection of the spectra previously calculated for AGN, starbursts and HII regions (Contini & Viegas 2001a,b). The UV-optical lines appear in the left diagrams as in Fig. 2, while the IR spectrum is shown in the right diagrams. The line absolute flux scales are different in Figs. 3 and 4 in order to display even weak significative lines (e.g. $\text{[CII]} 156$ and $\text{[NII]} 203$) as well as the entire $\text{Ly}\alpha$ line.

In Fig. 3 the models are suitable to a narrow line region (NLR) of AGN, LINERs and LLAGNs. The spectra were calculated adopting a power law (pl) radiation (Contini & Viegas 2001a). We have chosen the parameter ranges close to those of the physical conditions near the GC, as those calculated in Paper I (e.g. preshock velocity $V_s = 100 \text{ km s}^{-1}$ and preshock density $n_0 = 100 \text{ cm}^{-3}$) and corresponding to different intensities of the flux (indicated on top of the right diagram spectra) from the active center and different geometrical thickness of the emitting nebula D . The top and bottom spectra refer to the matter bound and to the radiation bound cases, respectively. In particular, line absolute fluxes in $\text{erg cm}^{-2} \text{s}^{-1}$ are calculated adopting a power-law radiation with $\alpha_{UV} = -1.5$, $\alpha_X = -0.4$ and different F_ν . $V_s = 100 \text{ km s}^{-1}$, $n_0 = 100 \text{ cm}^{-3}$, $B_0 = 10^{-4} \text{ gauss}$ and $D = 10^{17} \text{ cm}$ (top diagrams), $D = 10^{19} \text{ cm}$ (bottom diagrams). It can

be noticed that D affects the low-ionization level and neutral line intensity.

In Fig. 4 the spectra are calculated adopting a black body (BB) flux for different ionization parameters U (indicated on top of the right diagram spectra). The models are suitable to starbursts and HII regions (Contini & Viegas 1991b). In particular, line absolute fluxes in $\text{erg cm}^{-2} \text{s}^{-1}$ are calculated adopting a black body radiation, different U , $V_s = 100 \text{ km s}^{-1}$, $n_0 = 100 \text{ cm}^{-3}$, $B_0 = 10^{-4} \text{ gauss}$, $D = 10^{19} \text{ cm}$, and $T_* = 5 \cdot 10^4 \text{ K}$ (bottom diagrams), $T_* = 10^4 \text{ K}$ (top diagrams).

The top and bottom diagrams correspond to different colour temperatures of the stars which affect intermediate- and high-ionization level lines.

The $\text{Ly}\alpha$ line is the strongest in Fig. 3 and 4 spectra. Moreover, the fine structure lines emitted by several species in various ionization stages in the FIR ($\text{[CII]} 156$, $\text{[OI]} 63$, 145 , $\text{[NII]} 122$, $\text{[OIII]} 88$, 51 , $\text{[NIII]} 57$) are the strongest lines in the IR spectrum of most galaxies (Maiolino et al. 2009).

2.1 Mid-IR lines

We start with the analysis of the mid-IR lines, because they were observed.

It was argued in Paper I that the spectra near the GC show relatively strong low- and intermediate- ionization level lines which do not exclude a power-law dominated flux from a weak central black hole. Therefore, the lines are compared with those emitted from LINERs and low ionization AGN. In Fig. 5 we compare the Spitzer observations of $\text{[OIV]} 26 \mu\text{m} / \text{[NeII]} 12.8 \mu\text{m}$ versus $\text{[NeIII]} 15.5 \mu\text{m} / \text{[NeII]} 12.8 \mu\text{m}$ collected for a large sample of LINERs by Dudik et al. (2009) with the data observed by Simpson et al (2007) near the GC. We will use in the present figure and in the following ones the numbered positions observed across the GC region (Fig. 1 top), with an emphasis on those positions closest to the two major stellar clusters. Therefore, the data referring to the GC cover a rather extended area of the diagrams depending on the line ratios considered.

In Fig. 5 the Galactic line ratios to [NeII] appear towards the lower tail of the distribution, indicating a lower ionization level of the emitting gas. However, these ratios involve $\text{[OIV]}/\text{[NeII]}$. In particular, the intensity of the [OIV] line is strongly affected by V_s , as found in Paper I.

Model calculations show that the $\text{[NeV]}/\text{[NeII]}$ ratios are all $< 10^{-6}$ because V_s and U , which are the parameters responsible of heating and ionizing the gas, are relatively low. Therefore, the [NeV] lines are omitted in Table 3.

The general models (black asterisks connected by a solid line for a BB flux and black crosses connected by a solid line for a pl flux) are also displayed on Fig. 5. Comparison with starburst galaxies (BB models, Contini & Viegas 2001b) show that the [NeV] lines are relatively high for $T_* = 10^5 \text{ K}$, $U \geq 1$ and $V_s \geq 100 \text{ km s}^{-1}$. In shock dominated nebulae, the [NeV] lines are strong for $V_s \geq 200 \text{ km s}^{-1}$, and in AGNs (corresponding to pl dominated models, Contini & Viegas 2001a) they appear even for $V_s = 100 \text{ km s}^{-1}$ and $F_h \geq 10^{10} \text{ cm}^{-2} \text{s}^{-1} \text{ eV}^{-1}$. Nevertheless, the input parameters would correspond to higher V_s ($> 100 \text{ km s}^{-1}$) and higher n_0 ($> 100 \text{ cm}^{-3}$).

Summarizing, Fig. 5 suggests that the mid-IR line ratios near the GC are different from those of LINERs and

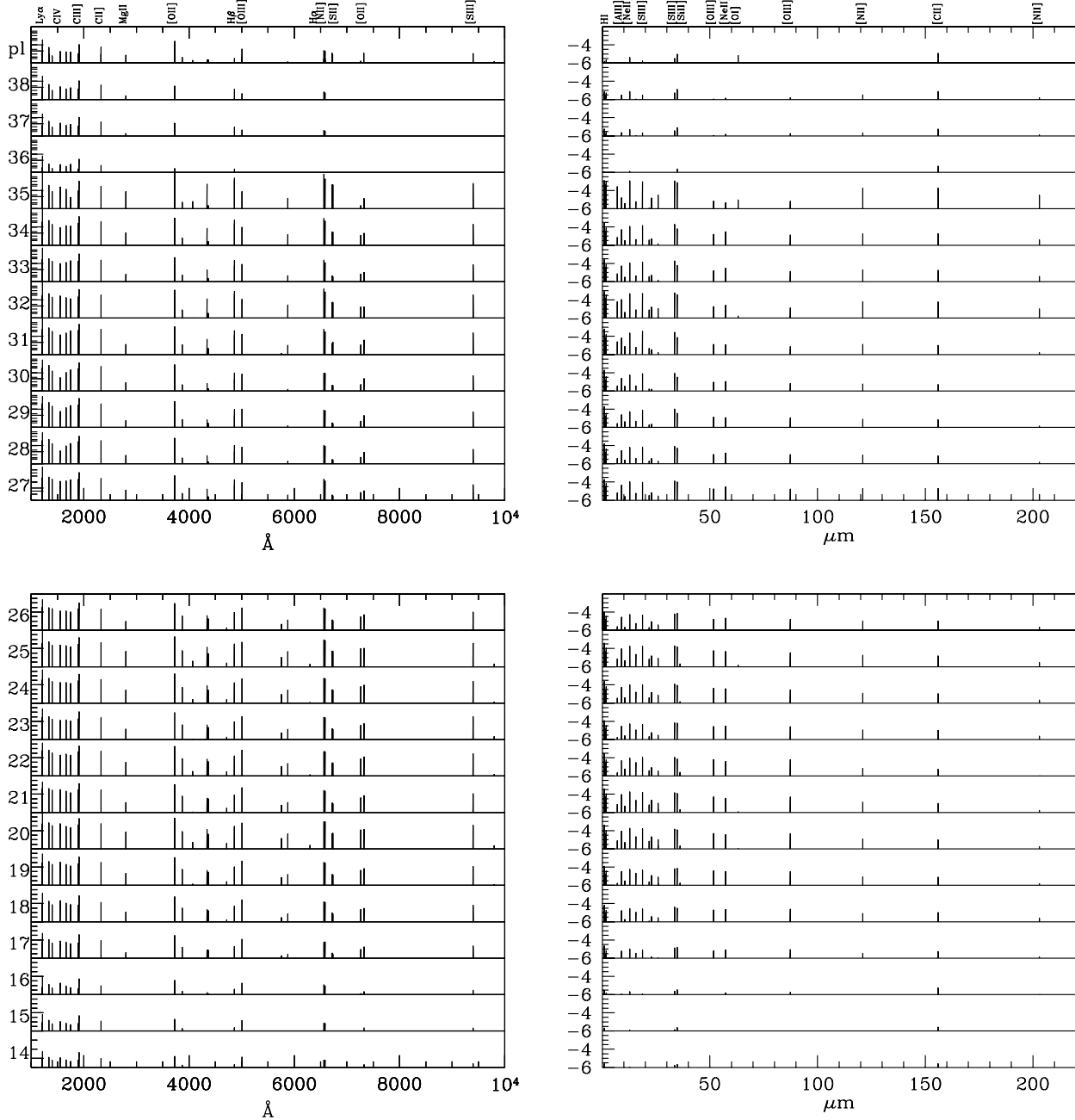


Figure 2. UV-optical-IR lines calculated (in $\text{erg cm}^{-2} \text{s}^{-1}$) by models m1-m38 and m_{pl} (Contini 2009) corresponding to the observed positions (Simpson et al (2007)).

starbursts. Comparison with models shows that the LINER data are located between the BB and pl dominated models indicating an hybrid character. The modelling shows that the GC data are dominated by BB flux.

2.2 Far-IR lines

Far-IR (FIR) lines deserve consideration, even if there were no possible FIR observations at the positions of Simpson et al, because the intensity of fine structure lines is proportional to the heating rate, which is given by the UV radiation field of young stars, in star-forming galaxies. The cumula-

tive intensity of the strongest FIR lines is proportional to the star forming rate (Kaufman et al 1999). Walter et al (2009) show that the [CII] line is a critical tracer of star formation in the first galaxies. The relative intensity of FIR lines gives information on metallicity of the ISM (Nagao et al), the density of the UV radiation field (Kaufman et al 1999), on the hardness of such field, and AGN versus starburst excitation (Spinoglio et al 2005).

The [CII] 156 line can provide a powerful cosmological tool to detect and characterize high- z galaxies. Capak et al (2009) claim that a very promising means of confirming object redshifts is through [CII] because [CII] 156 line is the

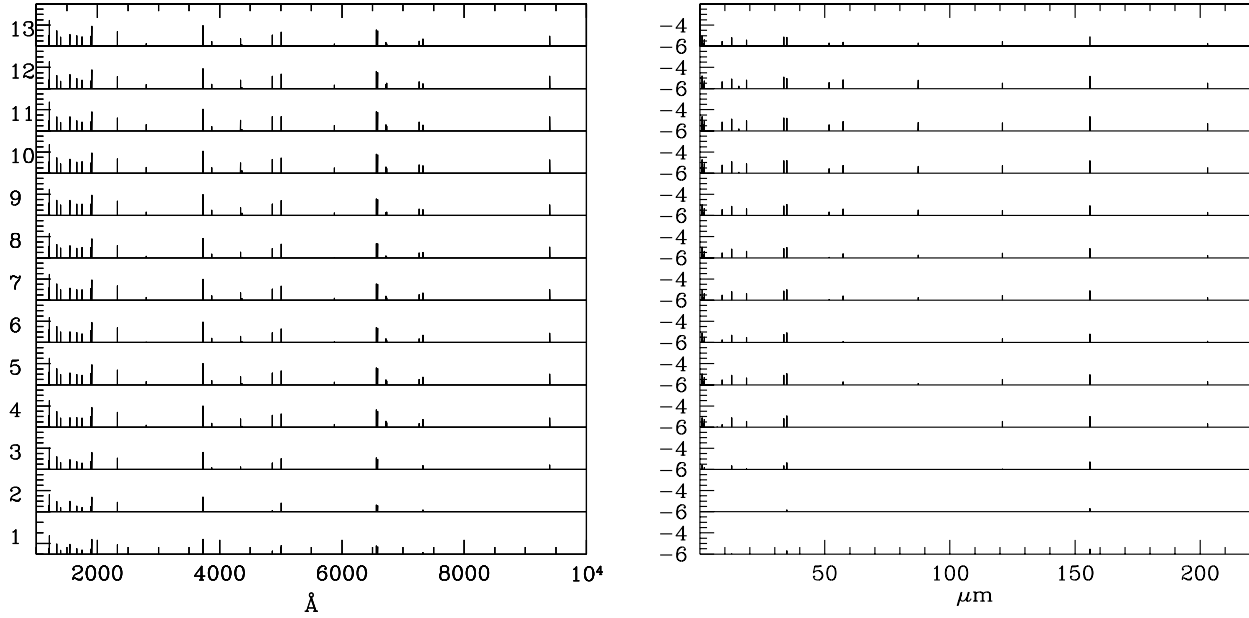


Figure 2 – continued

Table 1. UV lines ($\text{erg cm}^{-2} \text{s}^{-1}$)

position λ (Å)	SiIII 1206	Ly α 1215	CH 1335	SiIV 1397	CIV 1549	OIII] 1663	NIII] 1750	SiIII] 1892	CIII] 1909	CII] 2326	MgII 2798
1	3.87D-6	5.32D-5	8.98D-6	2.24D-6	8.41D-6	3.29D-6	2.43D-6	2.90D-6	2.39D-5	7.67D-6	2.9D-7
2	4.24D-6	4.03D-5	9.23D-6	2.51D-6	9.91D-6	3.46D-6	2.52D-6	3.20D-6	2.48D-5	7.94D-6	4.7D-7
3	7.64D-6	1.03D-4	1.56D-5	4.60D-6	8.81D-6	5.27D-6	3.90D-6	5.58D-6	4.10D-5	1.19D-5	4.3D-7
4	1.36D-5	3.25D-4	3.04D-5	7.28D-6	8.19D-6	7.80D-6	6.89D-6	1.00D-5	7.28D-5	2.54D-5	1.5D-6
5	1.69D-5	3.24D-4	3.38D-5	9.49D-6	1.36D-5	9.49D-6	7.80D-6	1.23D-5	8.06D-5	2.46D-5	2.0D-6
6	1.79D-5	2.13D-4	3.24D-5	9.79D-6	1.05D-5	8.88D-6	6.64D-6	1.29D-5	7.72D-5	2.38D-5	1.1D-6
7	1.67D-5	2.75D-4	3.30D-5	9.46D-6	1.42D-5	9.79D-6	9.90D-6	1.19D-5	8.08D-5	2.28D-5	1.8D-6
8	1.39D-5	1.86D-4	1.87D-5	8.25D-6	1.40D-5	8.10D-6	9.75D-6	9.52D-6	6.19D-5	1.44D-5	1.4D-6
9	1.66D-5	3.00D-4	2.76D-5	1.01D-5	2.69D-5	1.19D-5	1.20D-5	1.19D-5	8.68D-5	2.21D-5	2.1D-6
10	1.30D-5	4.86D-4	2.80D-5	7.80D-6	2.12D-5	1.10D-5	1.20D-5	9.40D-6	8.40D-5	2.28D-5	3.5D-6
11	9.90D-6	5.26D-4	2.02D-5	6.38D-6	2.18D-5	9.24D-6	6.60D-6	7.04D-6	6.58D-5	1.63D-5	3.9D-6
12	7.42D-6	3.36D-4	1.68D-5	4.90D-6	2.10D-5	8.82D-6	6.02D-6	5.18D-6	5.88D-5	1.33D-5	2.4D-6
13	1.17D-5	2.78D-4	2.86D-5	7.37D-6	1.35D-5	9.68D-6	7.70D-6	8.58D-6	7.90D-5	2.37D-5	1.7D-7
14	9.28D-6	5.60D-5	1.26D-5	6.40D-6	1.23D-5	6.60D-6	4.60D-6	6.40D-6	4.56D-5	9.60D-6	3.2D-7
15	9.55D-6	6.29D-5	1.50D-5	6.23D-6	1.09D-5	6.80D-6	4.91D-6	6.60D-6	4.91D-5	1.16D-5	3.4D-7
16	6.66D-6	9.58D-5	1.30D-5	5.37D-6	1.92D-5	8.88D-6	5.55D-6	4.14D-6	5.51D-5	9.25D-6	5.2D-7
17	6.77D-5	5.04D-4	1.08D-4	4.48D-5	7.56D-5	5.29D-5	3.74D-5	4.63D-5	3.73D-4	8.28D-5	4.0D-6
18	9.31D-5	1.28D-3	1.74D-4	7.20D-5	2.03D-4	1.11D-4	7.35D-5	6.17D-5	7.15D-4	1.33D-4	1.1D-5
19	3.07D-4	2.64D-3	3.90D-4	1.90D-4	3.60D-4	1.90D-4	1.33D-4	2.20D-4	1.31D-3	3.03D-4	2.0D-5
20	5.80D-4	7.34D-3	6.84D-4	3.45D-4	5.92D-4	2.81D-4	2.12D-4	4.03D-4	2.12D-3	5.42D-4	7.0D-5
21	4.20D-4	2.14D-3	3.92D-4	2.72D-4	3.23D-4	2.08D-4	1.48D-4	2.84D-4	1.46D-3	2.88D-4	1.2D-5
22	6.24D-4	4.13D-3	6.71D-4	3.39D-4	1.90D-4	2.50D-4	1.98D-4	4.37D-4	2.02D-3	5.07D-4	3.0D-5
23	2.82D-4	2.32D-3	3.26D-4	1.74D-4	1.32D-4	1.43D-4	1.09D-4	1.80D-4	1.12D-3	2.43D-4	1.4D-5
24	3.83D-4	4.34D-3	5.02D-4	2.18D-4	1.89D-4	1.80D-4	1.45D-4	2.70D-4	1.48D-3	3.91D-4	2.6D-5
25	3.97D-4	7.19D-3	5.42D-4	2.26D-4	2.34D-4	1.91D-4	1.51D-4	2.84D-4	1.56D-3	4.23D-4	4.6D-5
26	3.55D-4	2.27D-3	2.97D-4	2.25D-4	1.37D-4	1.28D-4	9.81D-5	2.21D-4	1.02D-3	2.04D-4	9.0D-6
27	3.03D-4	4.29D-3	3.43D-4	1.92D-4	1.24D-4	1.33D-4	1.75D-4	1.89D-4	1.11D-3	2.38D-4	1.3D-5
28	3.72D-4	2.59D-3	4.64D-4	1.60D-4	2.80D-5	9.20D-5	1.70D-4	2.60D-4	1.11D-3	3.37D-4	8.2D-6
29	4.14D-4	2.38D-3	5.36D-4	2.06D-4	5.85D-5	1.46D-4	2.52D-4	2.65D-4	1.52D-3	3.69D-4	5.4D-6
30	3.62D-4	2.48D-3	6.01D-4	1.49D-4	3.00D-5	1.04D-4	2.09D-4	2.68D-4	1.29D-3	4.59D-4	8.1D-6
31	6.40D-4	9.71D-3	8.03D-4	3.32D-4	1.48D-4	2.18D-4	3.90D-4	4.21D-4	1.29D-3	5.65D-4	1.3D-5
32	3.19D-4	2.01D-2	4.62D-4	1.93D-4	2.77D-4	1.68D-4	1.34D-4	2.10D-4	1.39D-3	3.36D-4	3.8D-7
33	2.84D-4	4.84D-3	3.32D-4	1.70D-4	1.00D-4	1.26D-4	2.00D-4	1.70D-4	1.10D-3	2.20D-4	6.4D-6
34	3.71D-4	1.28D-2	5.14D-4	1.91D-4	8.69D-5	1.38D-4	1.27D-4	2.44D-4	1.38D-3	3.76D-4	2.3D-5
35	1.38D-4	5.47D-2	3.68D-4	8.05D-5	2.53D-4	1.38D-4	1.84D-5	8.74D-5	1.06D-3	2.92D-4	7.6D-5
36	3.63D-6	6.03D-5	8.05D-6	2.76D-6	7.31D-6	4.37D-6	7.59D-6	2.30D-6	2.90D-5	5.52D-6	2.8D-7
37	1.58D-5	2.45D-4	3.87D-5	8.80D-6	2.64D-5	1.41D-5	1.85D-5	1.20D-5	1.07D-4	3.26D-5	1.8D-6
38	1.74D-5	3.60D-4	4.29D-5	9.78D-6	2.55D-5	1.45D-5	1.88D-5	1.34D-5	1.11D-4	3.75D-5	2.6D-6
pl	1.23D-5	3.44D-4	5.32D-5	6.13D-6	1.91D-5	1.64D-5	1.61D-5	1.07D-5	1.03D-4	5.63D-5	7.3D-6

dominant gas cooling line in the interstellar medium, traces the cold neutral medium and photon-dominated regions at the interface with active star forming regions, and is now routinely detected at $z > 4$ with existing sub-mm telescopes (Maiolino et al. 2009, 2005).

Luminous FIR galaxies typically have high dust-to-gas ratios. To distinguish between silicate or carbon grains the silicon features at 10 and 18 μm are observed. If the carbon

grain hypothesis prevails, this could explain unusually weak [CII] lines indicating that carbon is locked into dust grains. However, the high- z galaxies have enhanced [CII] emission by nearly an order of magnitude. At high redshift [CII] is detected in the sub-mm, in the host galaxies of QSR with $L(\text{IR}) > 10^{12}$ (ULIRGS). High- z star-forming galaxies are observed to have lower gas-metallicity than local galaxies (Maiolino et al 2008). In the narrow line region (NLR) of

Table 2. Optical lines ($\text{erg cm}^{-2} \text{s}^{-1}$)

P A	[OII] 3727+	[NeIII] 3869+	[SII] 4070+	HI 4340	[OIII] 4363	[AIV] 4713	H β 4861	[OIII] 5007+	[NII] 5755	HeI 5876	[OI] 6300+	H α 6563	[NII] 6583+	[SII] 6717	[SII] 6731	[AIII] 7262	[OII] 7322+
1	2.4D-5	8.6D-7	2.4D-8	8.4D-7	4.7D-7	4.9D-8	1.9D-6	6.3D-6	1.5D-7	2.6D-7	3.0D-8	5.9D-6	4.9D-6	3.9D-7	2.8D-7	5.0D-7	1.4D-6
2	2.4D-5	8.8D-7	2.7D-8	5.8D-7	4.7D-7	5.1D-8	1.3D-6	6.5D-6	1.5D-7	1.8D-7	2.3D-8	4.2D-6	3.9D-6	3.6D-7	2.4D-7	4.2D-7	1.5D-6
3	4.1D-5	1.4D-6	5.1D-8	1.8D-6	7.4D-7	7.8D-8	3.9D-6	1.1D-5	2.3D-7	5.5D-7	3.5D-8	1.2D-5	9.3D-6	9.0D-7	6.2D-7	9.4D-7	2.4D-6
4	9.6D-5	2.3D-6	1.6D-7	6.1D-6	1.2D-6	1.2D-7	1.4D-5	1.7D-5	5.4D-7	1.8D-6	9.5D-8	4.1D-5	3.1D-5	3.6D-6	2.6D-6	2.2D-6	5.1D-6
5	1.0D-4	2.6D-6	1.4D-7	6.0D-6	1.3D-6	1.3D-7	1.3D-5	2.0D-5	5.2D-7	1.8D-6	9.1D-8	3.9D-5	3.5D-5	3.1D-6	2.2D-6	3.2D-6	5.1D-6
6	8.6D-5	2.5D-6	1.2D-7	3.7D-6	1.2D-6	1.2D-7	8.3D-6	1.9D-5	5.0D-7	1.2D-6	6.6D-8	2.5D-5	2.3D-5	2.3D-6	1.6D-6	2.2D-6	4.9D-6
7	9.3D-5	2.6D-6	1.1D-7	5.1D-6	1.4D-6	1.4D-7	1.1D-5	2.1D-5	5.2D-7	1.5D-6	8.5D-8	3.3D-5	3.1D-5	2.4D-6	1.7D-6	3.3D-6	4.8D-6
8	6.7D-5	2.2D-6	8.9D-8	3.4D-6	1.1D-6	7.4D-8	7.4D-6	1.9D-5	3.4D-7	1.1D-6	5.2D-8	2.2D-5	2.2D-5	1.6D-6	1.2D-6	2.9D-6	3.2D-6
9	9.5D-5	3.2D-6	1.1D-7	5.5D-6	1.7D-6	1.2D-7	1.2D-5	2.6D-5	4.8D-7	1.8D-6	9.6D-8	3.6D-5	3.2D-5	2.0D-6	2.1D-6	4.0D-6	3.5D-6
10	1.2D-4	3.3D-6	1.9D-7	9.7D-6	1.7D-6	1.3D-7	2.1D-5	2.7D-5	6.1D-7	3.1D-6	1.5D-7	6.3D-5	5.4D-5	4.0D-6	2.8D-6	6.1D-6	5.0D-6
11	1.1D-4	2.6D-6	1.5D-7	1.0D-5	1.3D-6	1.3D-7	2.2D-5	2.2D-5	5.1D-7	3.2D-6	1.3D-7	6.5D-5	5.8D-5	3.8D-6	2.7D-6	6.8D-6	3.5D-6
12	7.4D-5	2.5D-6	1.1D-7	6.3D-6	1.2D-6	1.2D-7	1.4D-5	2.2D-5	3.6D-7	2.1D-6	9.6D-8	4.1D-5	3.4D-5	2.5D-6	3.2D-6	4.4D-6	2.9D-6
13	9.0D-5	2.7D-6	1.1D-7	5.0D-6	1.4D-6	1.3D-7	1.1D-5	2.1D-5	5.1D-7	1.6D-6	9.4D-8	3.3D-5	2.8D-5	2.3D-6	1.6D-6	3.1D-6	4.8D-6
14	1.6D-5	1.8D-6	3.9D-8	8.9D-7	9.3D-7	9.3D-8	2.0D-6	1.4D-5	2.0D-7	2.9D-7	2.0D-8	6.2D-6	6.2D-6	4.5D-7	3.2D-7	9.7D-7	2.0D-6
15	1.9D-5	1.8D-6	3.3D-8	9.9D-7	9.7D-7	9.7D-8	2.2D-6	1.4D-5	2.4D-7	3.2D-7	2.6D-8	7.0D-6	7.0D-6	4.4D-7	3.0D-7	9.7D-7	2.4D-6
16	3.6D-5	2.3D-6	3.0D-8	1.7D-6	1.3D-6	1.3D-7	3.7D-6	1.8D-5	1.9D-7	5.6D-7	3.7D-8	1.1D-5	9.0D-6	5.7D-7	3.9D-7	1.3D-6	2.0D-6
17	3.0D-4	1.5D-5	2.9D-7	8.1D-6	7.6D-6	7.0D-7	1.8D-5	1.2D-4	1.8D-6	2.7D-6	2.3D-7	5.6D-5	6.0D-5	3.8D-6	2.8D-6	8.8D-6	1.8D-5
18	5.3D-4	3.2D-5	6.4D-7	2.2D-5	1.6D-5	1.6D-6	4.9D-5	2.5D-4	2.9D-6	7.2D-6	4.9D-7	1.5D-4	1.4D-4	9.6D-6	7.2D-6	2.1D-5	3.0D-5
19	1.1D-3	5.5D-5	1.4D-6	4.5D-5	2.7D-5	2.6D-6	9.9D-5	4.5D-4	6.9D-6	1.5D-5	9.7D-7	3.0D-4	2.9D-4	1.6D-5	1.4D-5	4.3D-5	6.8D-5
20	2.3D-3	7.8D-5	5.2D-6	1.3D-4	4.1D-5	4.1D-6	2.9D-4	6.5D-4	1.4D-5	4.2D-5	2.4D-6	8.7D-4	9.4D-4	4.7D-5	5.2D-5	1.2D-4	1.4D-4
21	1.1D-3	6.1D-5	1.1D-6	3.7D-5	3.1D-5	2.8D-6	8.1D-5	5.0D-4	6.2D-6	1.2D-5	6.2D-7	2.5D-4	2.3D-4	1.1D-5	9.7D-6	3.9D-5	7.1D-5
22	1.8D-3	8.0D-5	3.1D-6	7.2D-5	3.7D-5	3.0D-6	1.6D-4	6.6D-4	1.1D-5	2.3D-5	1.4D-6	4.8D-4	4.6D-4	2.7D-5	2.7D-5	7.3D-5	1.3D-4
23	9.7D-4	4.1D-5	1.2D-6	4.1D-5	2.1D-5	1.8D-6	9.0D-5	3.3D-4	5.4D-6	1.3D-5	7.0D-7	2.7D-4	2.5D-4	1.6D-5	1.3D-5	3.6D-5	5.8D-5
24	1.6D-3	5.4D-5	2.6D-6	8.1D-5	2.7D-5	2.5D-6	1.7D-4	4.5D-4	8.8D-6	2.6D-5	1.2D-6	5.3D-4	4.8D-4	3.0D-5	2.7D-5	6.5D-5	9.6D-5
25	1.9D-3	5.7D-5	4.1D-6	1.3D-4	2.8D-5	2.6D-6	2.9D-4	4.8D-4	1.1D-5	4.3D-5	1.9D-6	8.8D-4	7.7D-4	5.2D-5	5.0D-5	9.7D-5	1.1D-4
26	8.4D-4	3.5D-5	1.0D-6	4.2D-5	1.8D-5	1.8D-6	9.1D-5	2.8D-4	4.5D-6	1.4D-5	5.2D-7	2.7D-4	2.3D-4	1.4D-5	1.1D-5	3.1D-5	5.2D-5
27	1.0D-3	3.7D-5	1.7D-6	8.1D-5	1.9D-5	1.7D-6	1.7D-4	2.9D-4	5.2D-6	2.6D-5	6.6D-7	5.3D-4	4.0D-4	2.8D-5	2.4D-5	4.4D-5	5.9D-5
28	1.3D-3	3.1D-5	2.0D-6	4.8D-5	1.5D-5	1.3D-6	1.1D-4	2.3D-4	7.4D-6	1.6D-5	7.0D-7	3.3D-4	2.9D-4	2.3D-5	2.1D-5	3.5D-5	8.8D-5
29	1.3D-3	4.4D-5	2.3D-6	4.0D-5	2.2D-5	1.8D-6	9.0D-5	3.2D-4	7.7D-6	1.4D-5	6.2D-7	2.8D-4	2.4D-4	2.3D-5	2.0D-5	3.2D-5	9.5D-5
30	1.4D-3	3.2D-5	3.4D-6	4.1D-5	1.5D-5	1.3D-6	9.1D-5	2.4D-4	9.1D-6	1.3D-5	7.6D-7	2.8D-4	2.8D-4	2.9D-5	2.8D-5	3.4D-5	1.1D-4
31	1.9D-3	6.4D-5	9.0D-6	1.8D-4	3.2D-5	2.2D-6	3.9D-4	4.7D-4	1.2D-5	5.8D-5	1.0D-6	1.2D-3	7.4D-4	8.6D-5	1.1D-4	6.2D-5	1.6D-4
32	2.0D-3	4.7D-5	1.0D-5	3.9D-4	2.4D-5	1.8D-6	8.4D-4	3.5D-4	1.0D-5	1.2D-4	1.7D-6	2.5D-3	1.5D-3	2.0D-4	1.9D-4	8.4D-5	8.4D-5
33	9.6D-4	3.5D-5	1.8D-6	9.2D-5	1.8D-5	1.2D-6	2.0D-4	2.7D-4	5.2D-6	3.1D-5	4.4D-7	6.0D-4	3.8D-4	3.0D-5	2.6D-5	4.2D-5	5.8D-5
34	1.7D-3	4.0D-5	7.4D-6	2.4D-4	2.0D-5	1.4D-6	5.3D-4	3.0D-4	9.5D-6	7.5D-5	1.1D-6	1.6D-3	1.0D-3	1.2D-4	1.2D-4	6.4D-5	9.8D-5
35	2.3D-2	3.5D-5	3.9D-5	1.1D-3	1.8D-5	1.9D-6	2.3D-3	2.5D-4	9.2D-6	7.4D-5	3.9D-6	6.9D-3	2.9D-3	1.0D-3	9.4D-4	1.8D-5	6.9D-5
36	2.0D-5	1.2D-6	1.8D-8	1.0D-6	6.2D-7	6.4D-8	2.3D-6	8.7D-6	1.1D-7	3.4D-7	3.2D-8	7.1D-6	5.0D-6	3.8D-7	2.6D-7	5.8D-7	1.2D-6
37	1.1D-4	4.1D-6	1.1D-7	4.0D-6	2.0D-6	1.4D-7	8.8D-6	3.0D-5	6.7D-7	1.3D-6	1.7D-7	2.8D-5	2.6D-5	1.8D-6	1.3D-6	3.0D-6	6.3D-6
38	1.3D-4	4.2D-6	1.6D-7	6.0D-6	2.1D-6	2.0D-7	1.3D-5	3.0D-5	7.8D-7	1.9D-6	3.1D-7	4.2D-5	3.6D-5	3.0D-6	2.2D-6	3.6D-6	7.1D-6
pl	2.4D-4	4.3D-6	2.0D-6	2.1D-6	2.4D-6	3.1D-7	3.1D-6	3.3D-5	1.1D-6	1.4D-6	9.4D-7	2.2D-5	2.1D-5	1.2D-5	9.0D-6	1.7D-6	1.2D-5

Table 3. IR lines ($\text{erg cm}^{-2} \text{s}^{-1}$)

position μm	[SIII] 0.94	[CI] 0.98	[SII] 1.03	HeI 1.08	HI 1.28	HI 2.34	[AII] 6.98	[AIII] 8.99	[SIV] 10.5	[NeII] 12.8	[NeIII] 15.6	[SIII] 18.7	[AIII] 21.8
1	9.5D-7	5.6D-8	2.2D-8	3.7D-7	3.2D-7	7.1D-7	9.9D-8	3.7D-7	3.0D-8	1.0D-6	1.2D-7	3.7D-7	2.8D-8
2	8.3D-7	5.1D-8	2.4D-8	2.6D-7	2.2D-7	4.9D-7	7.3D-8	2.4D-7	3.7D-8	6.9D-7	9.1D-8	2.8D-7	1.7D-8
3	2.7D-6	5.5D-8	4.7D-8	8.2D-7	6.7D-7	1.5D-6	2.1D-7	7.4D-7	7.0D-8	2.2D-6	1.8D-7	1.1D-6	5.6D-8
4	7.7D-6	1.3D-7	1.5D-7	2.6D-6	2.3D-6	5.2D-6	1.1D-6	1.8D-6	1.2D-7	7.6D-6	2.6D-7	3.5D-6	1.3D-7
5	1.1D-5	1.1D-7	1.3D-7	2.7D-6	2.2D-6	4.9D-6	6.5D-7	2.9D-6	1.3D-7	7.7D-6	3.8D-7	4.4D-6	2.1D-7
6	7.6D-6	8.3D-8	1.1D-7	1.7D-6	1.4D-6	3.2D-6	4.2D-7	1.7D-6	1.4D-7	4.8D-6	3.0D-7	3.1D-6	1.3D-7
7	1.0D-5	9.8D-8	1.1D-7	2.2D-6	1.9D-6	4.2D-6	4.2D-7	2.9D-6	1.4D-7	6.5D-6	5.0D-7	4.1D-6	2.1D-7
8	1.1D-5	5.2D-8	8.2D-8	1.6D-6	1.3D-6	2.8D-6	1.6D-7	2.4D-6	1.7D-7	4.5D-6	6.9D-7	4.0D-6	1.8D-7
9	1.0D-5	1.1D-7	9.5D-8	2.7D-6	2.1D-6	4.6D-6	3.3D-7	3.7D-6	1.6D-7	7.1D-6	9.8D-7	4.2D-6	2.7D-7
10	1.8D-5	1.7D-7	1.6D-7	4.3D-6	3.5D-6	7.9D-6	6.6D-7	5.8D-6	1.9D-7	1.2D-5	1.2D-6	7.9D-6	4.1D-7
11	2.2D-5	1.3D-7	1.5D-7	4.6D-6	3.7D-6	8.4D-6	5.9D-7	6.6D-6	2.0D-7	1.3D-5	1.5D-6	9.0D-6	4.8D-7
12	1.5D-5	9.6D-8	9.6D-8	3.0D-6	2.3D-6	5.2D-6	2.7D-7	4.4D-6	1.9D-7	7.8D-6	1.7D-6	6.3D-6	3.2D-7
13	9.2D-6	1.2D-7	1.1D-7	2.3D-6	1.9D-6	4.1D-6	4.0D-7	2.8D-6	1.4D-7	6.3D-6	6.1D-7	3.8D-6	2.1D-7
14	2.6D-6	3.0D-8	3.0D-8	4.3D-7	3.3D-7	7.3D-7	3.9D-8	6.1D-7	9.7D-8	1.1D-6	3.0D-7	8.9D-7	4.5D-8
15	2.1D-6	4.0D-8	2.9D-8	4.8D-7	3.7D-7	8.1D-7	5.7D-8	6.6D-7	7.7D-8	1.3D-6	2.9D-7	7.3D-7	4.8D-8
16	3.0D-6	4.4D-8	3.0D-8	8.1D-7	6.3D-7	1.4D-6	8.1D-8	1.1D-6	1.0D-7	2.0D-6	6.2D-7	1.2D-6	8.1D-8
17	2.2D-5	3.1D-7	2.7D-7	4.0D-6	3.1D-6	6.7D-6	3.4D-7	5.9D-6	7.0D-7	1.0D-5	3.5D-6	7.6D-6	4.3D-7
18	6.4D-5	5.9D-7	5.9D-7	1.1D-5	8.3D-6	1.8D-5	8.3D-7	1.6D-5	1.8D-6	2.7D-5	1.1D-5	2.4D-5	1.2D-6
19	1.2D-4	1.2D-6	1.2D-6	2.4D-5	1.7D-5	3.7D-5	1.7D-6	3.3D-5	3.0D-6	5.5D-5	2.1D-5	4.7D-5	2.4D-6
20	3.8D-4	2.3D-6	4.6D-6	7.5D-5	4.9D-5	1.1D-4	7.5D-6	9.0D-5	4.9D-6	1.8D-4	2.2D-5	1.5D-4	6.7D-6
21	1.2D-4	6.9D-7	1.1D-6	2.0D-5	1.4D-5	3.0D-5	1.1D-6	2.8D-5	3.9D-6	4.6D-5	1.8D-5	4.5D-5	2.0D-6
22	2.7D-4	1.5D-6	2.8D-6	4.1D-5	2.6D-5	5.8D-5	2.2D-6	5.3D-5	5.9D-6	8.9D-5	3.1D-5	1.1D-4	3.9D-6
23	1.2D-4	7.7D-7	1.1D-6	2.1D-5	1.5D-5	3.3D-5	1.7D-6	2.9D-5	2.6D-6	5.2D-5	1.1D-5	4.6D-5	2.1D-6
24	2.3D-4	1.3D-6	2.3D-6	4.2D-5	3.0D-5	6.5D-5	3.5D-6	5.5D-5	3.8D-6	1.0D-4	1.7D-5	1.0D-4	4.0D-6
25	3.8D-4	2.0D-6	3.8D-6	7.0D-5	4.9D-5	1.1D-4	7.0D-6	9.0D-5	4.6D-6	1.7D-4	2.3D-5	1.7D-4	6.4D-6
26	1.0D-4	5.0D-7	8.6D-7	2.1D-5	1.5D-5	3.5D-5	2.5D-6	2.6D-5	2.1D-6	5.3D-5	5.6D-6	4.3D-5	1.9D-6
27	1.9D-4	6.1D-7	1.5D-6	3.8D-5	3.0D-5	6.6D-5	6.1D-6	4.5D-5	2.5D-6	1.0D-4	6.0D-6	9.1D-5	3.3D-6
28	1.6D-4	7.0D-7	1.8D-6	2.5D-5	1.8D-5	4.1D-5	3.9D-6	2.8D-5	2.5D-6	6.2D-5	4.0D-6	6.7D-5	2.0D-6
29	1.8D-4	5.6D-7	2.0D-6	2.1D-5	1.5D-5	3.4D-5	2.7D-6	2.4D-5	4.3D-6	5.2D-5	4.8D-6	7.7D-5	1.8D-6
30	1.9D-4	8.6D-7	3.0D-6	2.2D-5	1.5D-5	3.5D-5	3.5D-6	2.3D-5	3.4D-6	5.3D-5	3.6D-6	7.6D-5	1.6D-6
31	6.1D-4	7.4D-7	8.2D-6	9.4D-5	6.6D-5	1.5D-4	2.5D-6	6.4D-5	7.4D-6	2.2D-4	6.2D-6	3.5D-4	4.7D-6
32	8.1D-4	1.5D-6	9.2D-6	1.8D-4	1.5D-4	3.3D-4	6.4D-5	1.1D-4	4.4D-6	4.7D-4	8.4D-6	5.0D-4	7.6D-6
33	5.6D-4	3.0D-7	1.5D-6	4.5D-5	3.5D-5	7.7D-5	7.2D-6	5.0D-5	3.2D-6	1.1D-4	4.7D-6	1.4D-4	3.6D-6
34	2.3D-3	9.5D-7	6.9D-6	1.2D-4	9.3D-5	2.1D-4	4.0D-5	7.2D-5	3.4D-6	3.0D-4	4.4D-6	3.1D-4	5.1D-6
35	1.2D-3	3.5D-6	3.5D-5	1.1D-4	4.1D-4	9.1D-4	2.6D-4	1.6D-5	3.9D-6	1.2D-3	6.2D-6	9.0D-4	1.2D-6
36	1.1D-6	4.6D-8	1.7D-8	4.8D-7	4.0D-7	8.9D-7	9.9D-8	5.3D-7	4.1D-8	1.3D-6	2.1D-7	5.1D-7	3.9D-8
37	5.5D-6	2.6D-7	1.0D-7	1.8D-6	1.5D-6	3.3D-6	3.3D-7	2.3D-6	1.4D-7	4.9D-6	1.0D-6	2.1D-6	1.7D-7
38	7.0D-6	4.6D-7	1.5D-7	2.8D-6	2.3D-6	5.1D-6	6.4D-7	3.1D-6	1.3D-7	7.6D-6	1.1D-6	2.8D-6	2.2D-7
pl	1.1D-5	1.4D-6	1.4D-6	1.5D-6	8.5D-7	2.0D-6	8.5D-7	2.9D-6	6.1D-7	3.9D-6	1.1D-6	1.7D-6	2.2D-7

Table 4. IR lines ($\text{erg cm}^{-2} \text{s}^{-1}$)

position μm	[FeIII] 22.9	[OIV] 25.9	[FeII] 26.0	[SIII] 33.6	[SiII] 34.8	[NeIII] 36.1	[OIII] 51.7	[NIII] 57.3	[OI] 63.1	[OIII] 87.3	[NII] 121.5	[CII] 156.	[NII] 203.3
1	1.7D-8	3.4D-8	8.2D-8	6.9D-7	2.0D-6	1.1D-8	1.6D-7	2.4D-7	3.7D-8	2.6D-7	5.2D-7	2.9D-6	5.4D-7
2	1.8D-8	3.8D-8	9.2D-8	5.2D-7	1.4D-6	7.7D-9	1.3D-7	1.8D-7	2.6D-8	2.2D-7	3.5D-7	2.0D-6	3.6D-7
3	7.8D-8	3.9D-8	1.8D-7	2.1D-6	4.3D-6	1.6D-8	3.0D-7	5.4D-7	3.9D-8	5.0D-7	1.1D-6	5.1D-6	1.0D-6
4	1.9D-7	3.8D-8	3.8D-7	6.3D-6	1.2D-5	2.7D-8	4.5D-7	8.9D-7	1.1D-7	7.0D-7	3.5D-6	9.9D-6	2.1D-6
5	3.6D-7	5.7D-8	3.5D-7	8.1D-6	1.1D-5	3.9D-8	8.3D-7	1.9D-6	7.8D-8	1.3D-6	3.2D-6	8.7D-6	2.0D-6
6	3.3D-7	4.6D-8	3.8D-7	5.6D-6	8.1D-6	2.5D-8	6.0D-7	1.2D-6	5.8D-8	9.1D-7	2.2D-6	6.0D-6	1.3D-6
7	4.1D-7	5.9D-8	3.5D-7	7.4D-6	9.6D-6	4.4D-8	1.1D-6	2.4D-6	6.6D-8	1.8D-6	2.8D-6	7.5D-6	1.7D-6
8	4.2D-7	6.1D-8	1.9D-7	7.4D-6	6.2D-6	6.0D-8	1.7D-6	3.5D-6	3.7D-8	2.8D-6	1.8D-6	6.1D-6	1.4D-6
9	6.5D-7	1.1D-7	5.3D-7	7.7D-6	1.1D-5	8.6D-8	2.1D-6	3.9D-6	8.6D-8	3.4D-6	3.0D-6	8.5D-6	2.0D-6
10	5.2D-7	9.3D-8	4.3D-7	1.4D-5	1.5D-5	1.0D-7	2.7D-6	5.4D-6	1.4D-7	4.3D-6	5.2D-6	1.5D-5	3.5D-6
11	7.9D-7	9.0D-8	4.6D-7	1.7D-5	1.6D-5	1.3D-7	3.7D-6	7.7D-6	1.3D-7	6.2D-6	5.7D-6	2.2D-5	4.8D-6
12	5.2D-7	8.8D-8	3.0D-7	1.2D-5	9.0D-6	1.4D-7	3.6D-6	6.4D-6	8.2D-8	6.0D-6	3.3D-6	1.4D-5	3.2D-6
13	3.8D-7	5.7D-8	4.8D-7	7.1D-6	6.9D-6	5.4D-8	1.9D-6	2.3D-6	8.7D-8	1.9D-6	2.7D-6	8.4D-6	1.9D-6
14	1.9D-7	5.1D-8	1.4D-7	1.7D-6	2.1D-6	2.8D-8	5.9D-7	9.9D-7	1.2D-8	1.0D-6	4.7D-7	2.5D-6	5.1D-7
15	2.0D-7	4.6D-8	2.2D-7	1.4D-6	2.4D-6	2.6D-8	5.3D-7	8.6D-7	1.8D-8	8.8D-7	5.5D-7	2.7D-6	5.5D-7
16	2.8D-7	8.1D-8	3.3D-7	2.3D-6	3.3D-6	5.5D-8	1.0D-6	1.5D-6	3.3D-8	1.7D-6	9.2D-7	5.3D-6	1.0D-6
17	1.4D-6	3.2D-7	1.1D-6	1.3D-5	1.5D-5	3.1D-7	6.3D-6	8.1D-6	1.4D-7	8.8D-6	3.3D-6	5.4D-6	1.3D-6
18	3.7D-6	8.8D-7	2.7D-6	4.0D-5	3.2D-5	9.8D-7	2.0D-5	2.2D-5	3.4D-7	2.5D-5	7.7D-6	1.0D-5	2.5D-6
19	1.2D-5	1.5D-6	7.5D-6	6.4D-5	7.4D-5	1.8D-6	3.9D-5	3.2D-5	5.9D-7	3.3D-5	8.4D-6	7.8D-6	1.6D-6
20	2.1D-5	2.3D-6	1.0D-5	1.4D-4	1.2D-4	2.0D-6	4.9D-5	3.5D-5	1.2D-6	4.9D-5	1.2D-5	9.6D-6	1.7D-6
21	1.1D-5	1.4D-6	3.3D-6	6.1D-5	5.4D-5	1.5D-6	4.3D-5	3.6D-5	2.4D-7	3.6D-5	6.1D-6	5.6D-6	1.2D-6
22	8.4D-6	8.3D-7	3.4D-6	1.1D-4	7.3D-5	2.7D-6	6.4D-5	3.9D-5	6.2D-7	6.4D-5	7.0D-6	5.5D-6	1.0D-6
23	5.8D-6	5.9D-7	3.0D-6	6.9D-5	6.4D-5	9.9D-7	2.7D-5	3.1D-5	4.5D-7	2.7D-5	1.1D-5	1.0D-5	2.3D-6
24	1.5D-5	8.2D-7	7.0D-6	1.2D-4	9.4D-5	1.4D-6	4.2D-5	3.8D-5	7.0D-7	3.0D-5	1.2D-5	1.0D-5	2.1D-6
25	1.5D-5	9.9D-7	8.4D-6	2.0D-4	1.5D-4	2.0D-6	5.5D-5	4.8D-5	1.4D-6	3.5D-5	1.8D-5	1.5D-5	2.9D-6
26	8.6D-6	6.0D-7	3.8D-6	6.4D-5	7.6D-5	4.5D-7	1.6D-5	2.2D-5	2.7D-7	1.5D-5	1.0D-5	1.1D-5	2.3D-6
27	6.5D-6	5.2D-7	2.8D-6	1.3D-4	1.0D-4	5.2D-7	1.8D-5	2.9D-5	5.2D-7	1.8D-5	1.9D-5	1.9D-5	4.0D-6
28	3.7D-6	1.1D-7	1.8D-6	8.5D-5	5.3D-5	3.2D-7	1.1D-5	1.5D-5	3.2D-7	1.1D-5	8.6D-6	7.5D-6	1.5D-6
29	2.2D-6	2.3D-7	9.9D-7	1.0D-4	3.6D-5	4.5D-7	1.4D-5	1.2D-5	1.8D-7	1.2D-5	7.5D-6	6.8D-6	1.4D-6
30	1.5D-6	1.2D-7	9.1D-7	8.6D-5	3.3D-5	3.6D-7	9.1D-6	1.1D-5	2.7D-7	6.6D-6	5.5D-6	4.8D-6	8.6D-7
31	3.5D-6	6.2D-7	1.6D-6	2.7D-4	7.4D-5	3.9D-7	1.2D-5	1.2D-5	3.9D-7	7.4D-6	1.2D-5	9.8D-6	1.6D-6
32	1.6D-5	1.2D-6	1.1D-5	6.0D-4	3.6D-4	7.6D-7	1.8D-5	2.5D-5	1.7D-6	1.3D-5	6.3D-5	6.0D-5	1.0D-5
33	5.0D-6	4.2D-7	1.4D-6	1.9D-4	6.2D-5	4.0D-7	1.5D-5	3.0D-5	2.0D-7	1.4D-5	1.9D-5	1.8D-5	3.8D-6
34	4.7D-6	3.6D-7	2.6D-6	3.3D-4	1.6D-4	4.2D-7	1.1D-5	1.5D-5	1.1D-6	7.4D-6	3.1D-5	2.7D-5	4.5D-6
35	1.5D-5	9.7D-7	3.0D-5	1.1D-3	7.8D-4	4.6D-7	6.9D-6	4.6D-6	9.2D-6	6.9D-6	1.8D-4	1.9D-4	3.0D-5
36	3.0D-8	3.2D-8	1.3D-7	9.4D-7	2.3D-6	1.8D-8	2.5D-7	3.7D-7	4.4D-8	4.5D-7	6.3D-7	4.8D-6	8.0D-7
37	1.4D-7	1.1D-7	4.8D-7	3.8D-6	8.1D-6	8.8D-8	1.1D-6	1.5D-6	1.8D-7	1.8D-6	2.2D-6	5.6D-6	1.3D-6
38	1.0D-7	1.0D-7	5.2D-7	5.1D-6	1.3D-5	5.4D-8	1.1D-6	1.4D-6	3.8D-7	1.6D-6	3.2D-6	7.2D-6	1.6D-6
pl	3.1D-8	1.1D-7	6.6D-7	3.1D-6	9.4D-6	9.1D-8	5.5D-7	5.2D-7	6.8D-6	8.8D-7	9.7D-7	1.2D-5	6.4D-7

models correspond to HII regions, with star temperatures of $\sim 3 \cdot 10^4$ K and moderate shock velocities of $\sim 70 \text{ km s}^{-1}$. Calculated spectra for starburst and AGN (Figs. 3 and 4) show that the [CII] line intensity depends strongly on the physical conditions of the emitting gas. It prevails at low shock velocities in radiation dominated nebulae (large geometrical thickness) and for relatively low photoionization flux intensities in both the BB and power-law models.

2.3 Optical lines

We will discuss the spectra from regions near the GC in the UV and optical range by the line ratios presented in Tables 1 and 2, respectively. They were calculated using the models which explain the IR data. These calculated spectra are the most plausible substitute to the observational data.

Comparing the significant optical line ratios with those observed in HII regions, Seyfert galaxies, LINERs, etc. (Veilleux 1985, Veilleux & Osterbrock 1987, Ho et al. 1997) we obtain a further hint on the nature of the spectra observed near the GC.

The HeII 4686 and HeII 1640 lines are too weak to be observed near the GC. This is due to the relatively low ionization parameter U and the relatively low temperature of the stars T_* . The spectrum is similar to that of low luminous AGN (e.g. NGC 4579, Contini 2004). In fact the forbidden lines from the first and second ionization levels are strong : [OII] 3727, [OIII] 5007+ ([OII]3727/[OIII]5007 > 1) [NII] 6548+, [SII]6717+ in the optical range, and [SIII] 9400 in the NIR are present.

In Fig. 6 (top) the [OIII] 5007/H β versus [NII]/H α diagram shows the results obtained for the GC in the different positions (filled magenta circles). The diagram is divided

by the red lines in the zones characteristic of Seyfert (S), LINER (L), HII (H) regions following Veilleux et al (1987, Fig. 6a).

The GC data are scattered over the three zones. The data cover 38 different positions, each with a beam size of approximately 250 square arcsec, and therefore sample regions observed throughout a slit crossing a limited region near the GC. We compare them with 2" wide long slit spectra across the Seyfert 2 galaxy NGC 7130 (Contini et al 2002, Radovich et al. 1997) at position angles PA=90° and 160° and with the inner 6" long slit spectroscopy at PA=11° and a high resolution spectrum in a 2" X 4" region centered on the nucleus at PA=90° (Shields & Filippenko 1990). These data cover the entire galaxy including the active center and starburst regions, central and peripheral.

The slope of the line ratios determines the ionization source, however, the areas covered by Spitzer observations for the GC and for NGC 7130 are different by many orders of magnitude. At the distance of the GC (~ 8 Kpc) the LH IRS Spitzer beam size is $\sim 0.5 \text{ pc}^2$. At the distance of NGC 7130 (which SIMBAD gives as 68.58 Mpc), the beam size would be $\sim 1000 \text{ pc}^2$, dwarfing all of the GC observations. So we have integrated single emission lines throughout all the 38 positions adopting that the physical conditions of the filaments included in each of the observed areas are the same. The weights are calculated by $w = (0.5/\pi(D(pc))^2) \int f$ in each position. The values of the geometrical thickness of the emitting nebulae D , are given in Paper 1 (table 2), the filling factor $f=1$. The results are indicated as a large black dot on both Figs. 6 and 7 (top diagram). Notice that the ISM regions have a strong effect on the [OI]/H α line ratios because the models are matter bound.

The presence of a Seyfert nucleus and energetic star-

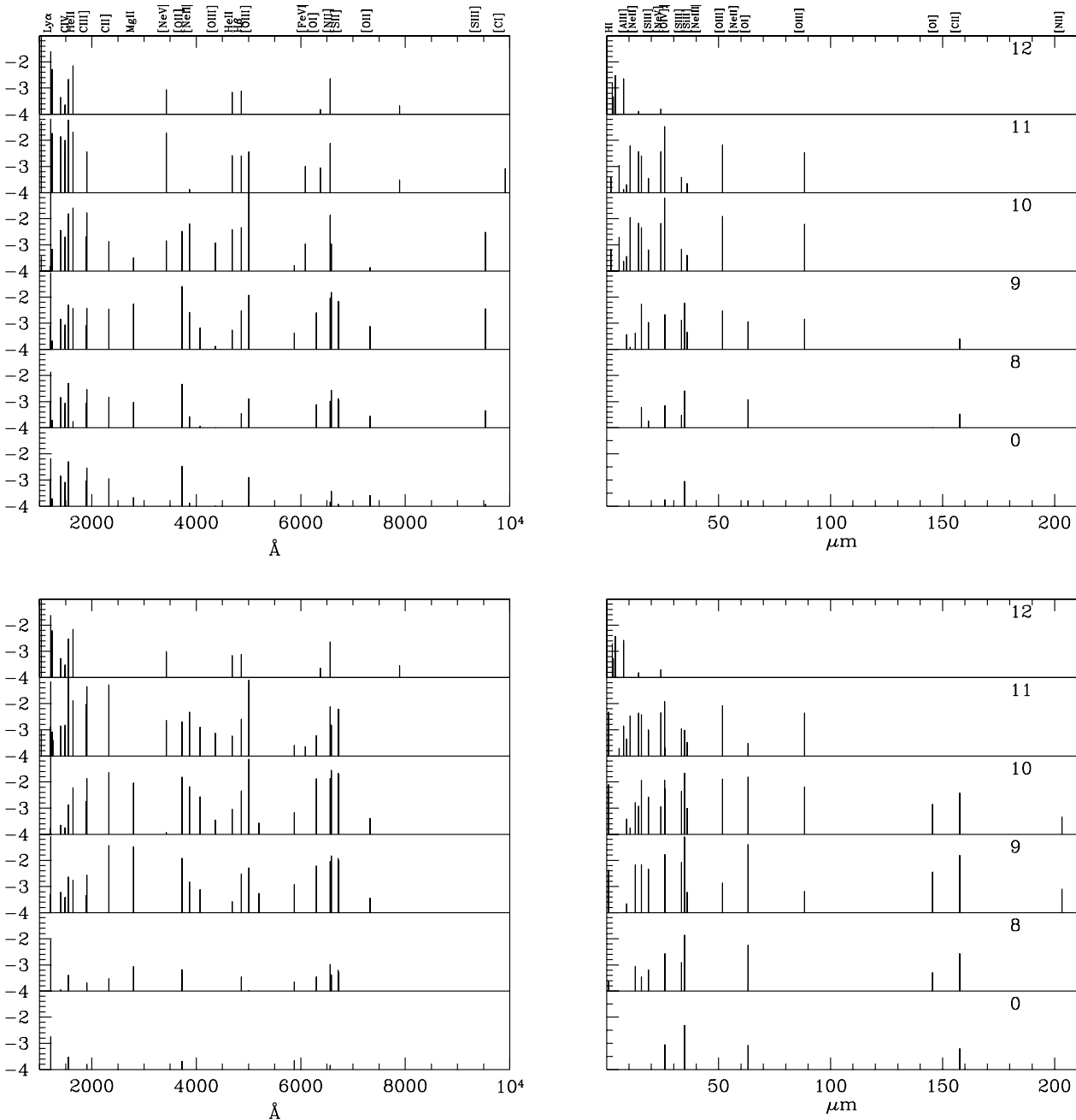


Figure 3. Model calculations of line fluxes adopting a pl flux (Contini & Viegas 2001a); see text

bursts are evident from the optical and near-IR properties of the galaxy. Therefore NGC 7130 is a remarkable prototype of a "composite" galaxy (Contini et al. 2002). The trend of the NGC 7130 data is roughly the same as that of the GC. However the data showing the maximum $[\text{OIII}]/\text{H}\beta$ observed in NGC7130 are not reproduced by the GC data. This confirms that the pl photoionizing flux in the central region of the Seyfert 2 galaxy is stronger than that predicted in the observed regions near the GC (Paper I, table 2). On the other hand, the BB radiation flux leads to $[\text{OIII}]/\text{H}\beta$ versus $[\text{NII}]/\text{H}\alpha$ line ratios similar to those of the nebulae close to starbursts. For a low ionization parameter U , the trend of the GC data in Fig. 6 (top diagram) recovers that of the

HII regions in the external regions of NGC 7130, far from the center, which are photoionized by a BB flux from the peripheral starburst stars.

The models (black lines) displayed on Fig. 6 (top diagram) confirm that the GC data imply $U < 0.01$. O/H and N/H relative abundances are about solar for the GC spectra because the models are calculated with solar abundances.

In the bottom diagram of Fig. 6 we show for comparison the diagnostic diagram for a sample of active galaxies assembled by Ho et al (1997, fig. 7a). The GC spectra would appear in the regions suited to HII (starburst galaxies).

In the bottom diagrams of Figs. 6, 7, and 8 we compare regions with very different extensions (notice for instance

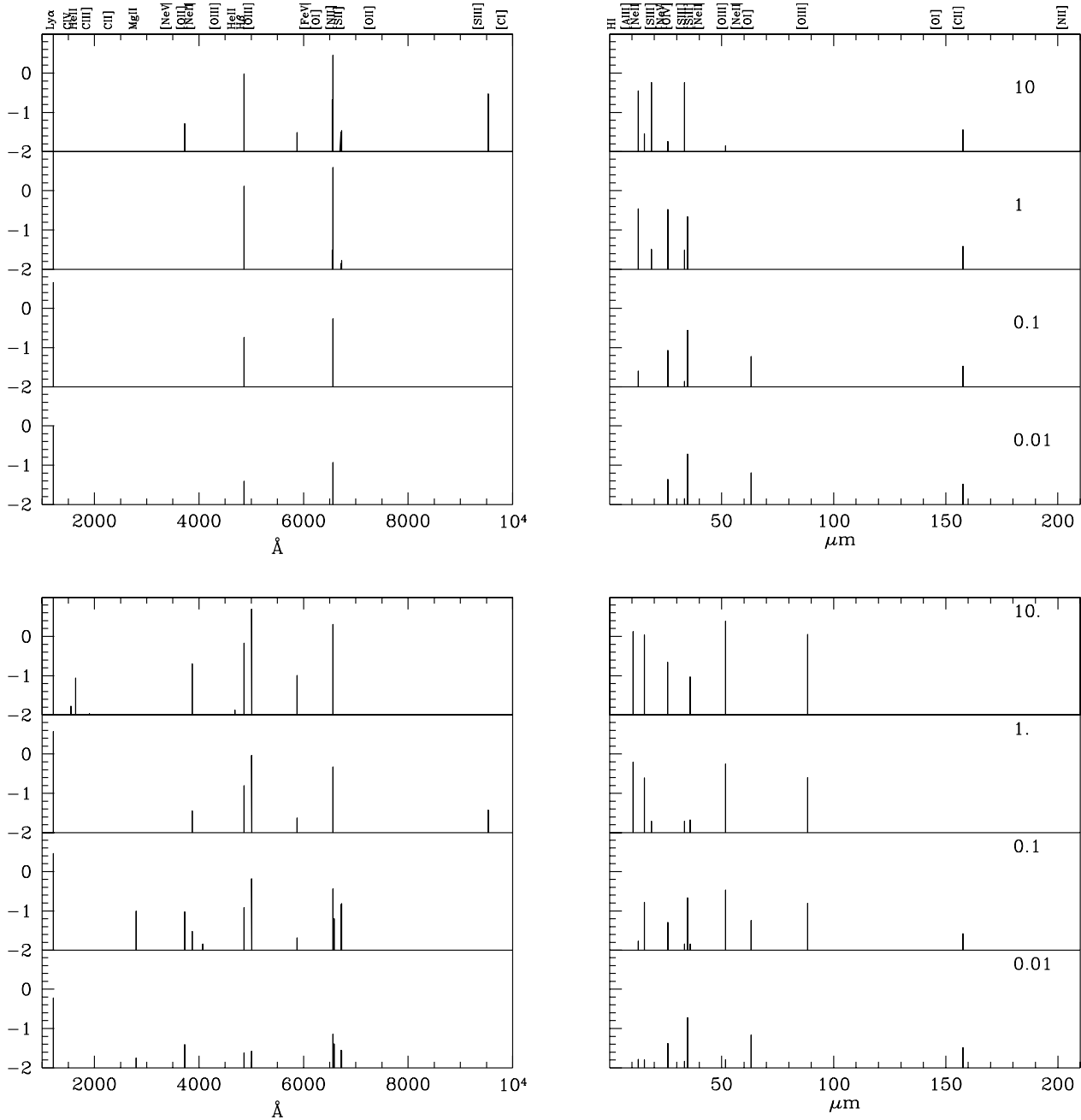


Figure 4. Model calculations of line fluxes adopting a BB flux (Contini & Viegas 2001b); see text

the scales in Fig. 1 top and bottom diagrams) and nature. The observations reported by Ho et al were taken with large amplitudes covering the entire galaxy. However, the dominant character common to a certain group of objects (AGN, starburst, LINER, etc) was confirmed by theoretical models. Therefore, we consider that these comparisons are sensible.

To constrain the results, we compare in Fig. 7 the $[\text{OIII}]/\text{H}\beta$ versus $[\text{OI}] 6300/\text{H}\alpha$ (top diagram) calculated for the GC with the data observed throughout NGC 7130. In the bottom diagram of Fig. 7 the diagnostic diagram of Ho et al (1997, fig 7c) is shown for comparison. The GC data show low $[\text{OI}]/\text{H}\alpha$. This confirms that the nebulae are filaments with relatively small geometrical thickness (D), as

calculated in Paper I, The fitting models are matter bound because the cooling rate in the post-shock region is low. The downstream edge of the nebula is reached before the gas cools to temperatures ($< 10^4$ K) low enough to recombine emitting the bulk of neutral lines.

This is an important issue revealing that matter is highly fragmented. It could be a result of Richtmyer-Meshkov (RM) (Mikaelian 1990; Graham & Zhang 2000) instability which is an interfacial instability between two fluids of different densities driven by weak and intermediate shock waves characteristically leading to photoionized "fingers". (For a discussion of the fragmentation generated by Kelvin-Helmholtz instabilities, see Sect. 3). The "ubiquitous

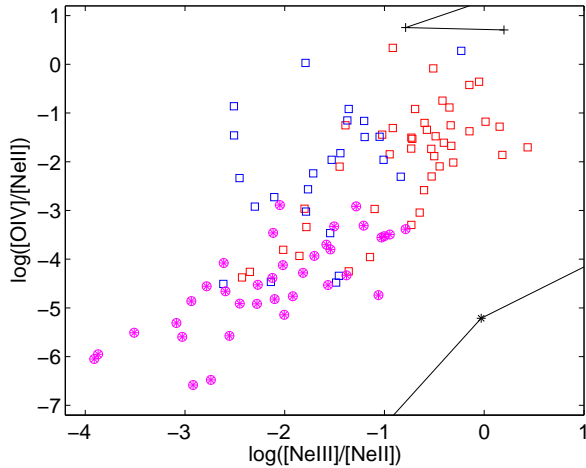


Figure 5. Mid-IR spectra: red squares and blue squares : IR-faint LINERs and IR-bright LINERs observations reported by Dudik et al. (2009), respectively. Magenta filled circles : the GC observation by Simpson et al (2007).

ISM filamentary structure” is confirmed by Molinari et al. (2010) by the Herschel Hi-GAL Milky Way survey. This suggests fragmentation which derives from a turbulent regime.

2.4 UV lines

The evolution of star forming galaxies and quasars has been investigated in the last years (e.g. Atek et al 2008 and references therein) through numerical simulations, focusing on the Ly α line which is considered the strongest observable line from high-redshift galaxies (Laursen 2009). The calculated spectra for AGN and starburst galaxies based on the models used in this paper are presented in Contini & Viegas (2001a,b). The low V_s , low n_0 models appear in graphical form in Figs. 3 and 4, respectively. The left diagrams in Figs. 3 and 4 show that Ly α is by far the strongest calculated UV line.

The models show that, although Ly α line always prevails, its ratio to the UV lines (e.g. CIII]1909) is lower for HII regions than for AGNs. However, recall that the spectra are calculated using cosmic abundances, so line ratios referring to different elements can be different, depending on the relative abundances.

Bertone et al (2009) claim that in the low redshift universe the Ly α forest may trace less than half the baryons. They suggest that the gravitational shocks, produced at the time of structure formation, progressively heat the diffuse intergalactic medium. Approximately half of the intergalactic gas is predicted to have temperatures in the range of 10^5 - 10^7 K at $z \sim 0$ which is too hot to emit or absorb hydrogen Ly α radiation. However, this shock heated gas (hot-warm IG medium) has not been unambiguously detected. Metal lines in the UV band could detect the cooler fraction of the hot-warm gas. The models presented by Contini & Viegas (2001a,b) accounting for the shocks give a hint on the ratio of UV lines to Ly α .

The CIV 1550 and Ly α line are the strongest in the UV from gas heated to 10^4 - 10^5 K by primary and secondary

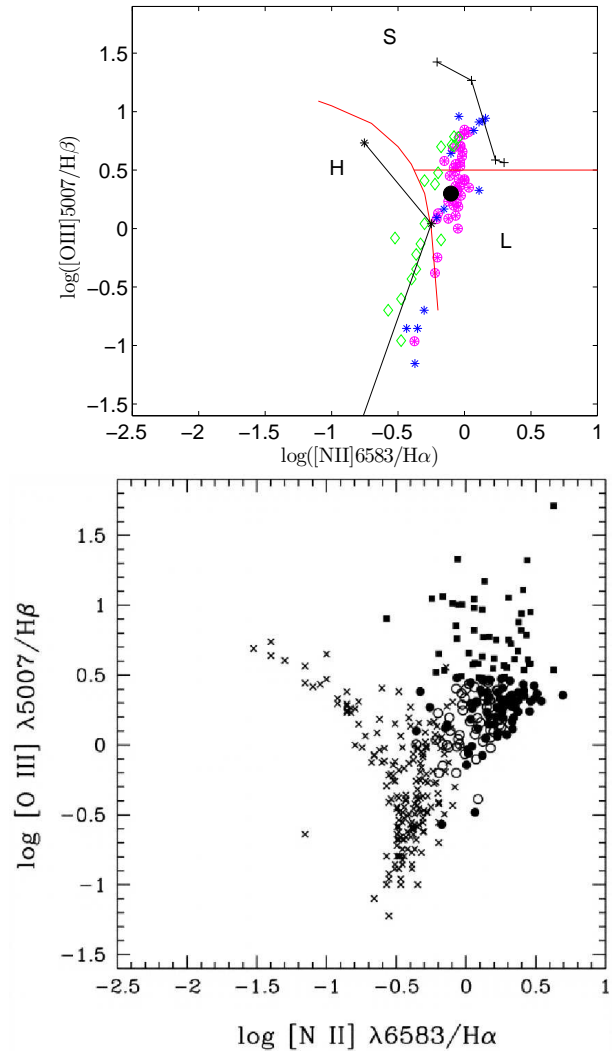


Figure 6. Top : comparison with observed line ratios. Magenta filled circles : model results for the Galaxy; ; blue stars : NGC 7130 (Radovich et al 1997); green open diamonds (Shield & Filippenko 1990). Bottom : [OIII]/H β versus [NII]/H α adapted from Ho et al (1997, fig. 7a) ; H II nuclei (crosses), Seyfert nuclei (squares), LINERs (filled circles), and transition objects (open circles).

radiation due to photoionization and emission from slabs heated by the shocks, respectively. This can be noticed in different objects such as AGN, starbursts, etc and, on a small scale, supernova remnants, novae, and symbiotic star systems etc. In the GC the CIII] 1909 multiplet is also important because photoionization is relatively low.

In Fig. 8 CIV/Ly α versus CIII]/Ly α is shown for the GC (top) and compared with NLS1 (Narrow Line Seyfert 1) and other type of galaxies (bottom) in the diagram presented by Kuraszkiewicz et al (2000, fig. 1). We have added in the top diagram the data in regions observed by Kraemer et al (2000) at different locations throughout the Seyfert 2 galaxy NGC 4151 (Contini et al 2002). The observed spectra were obtained by low-dispersion long-slit data, at a position angle P.A. = 221, using the Hubble Space Telescope Space Telescope Imaging Spectrograph, using a narrow slit width

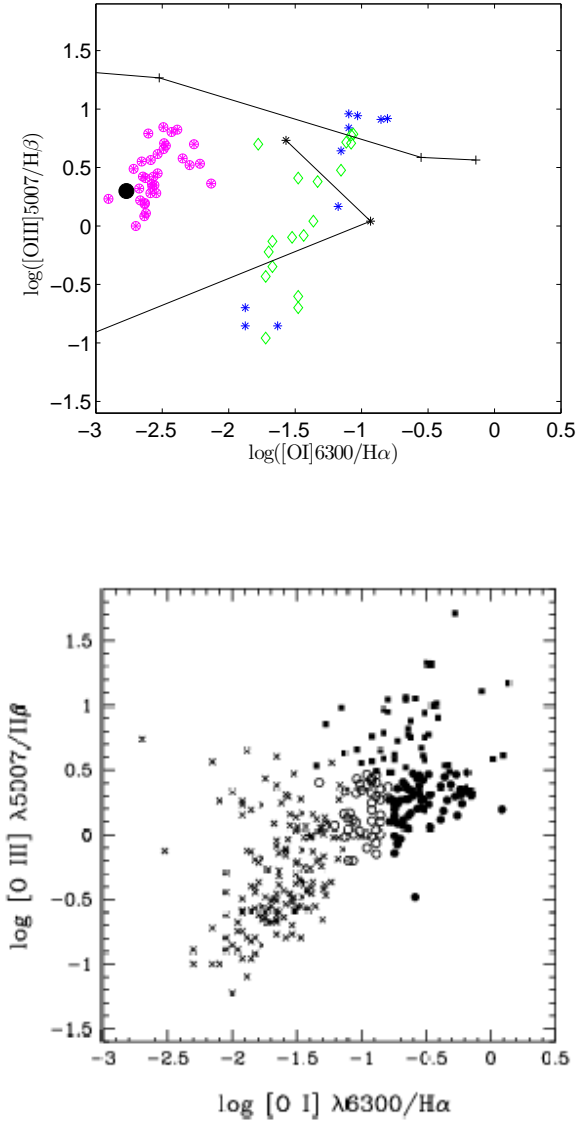


Figure 7. Top : comparison with observed line ratios. Magenta filled circles : model results for the Galaxy; ; blue stars : NGC 7130 (Radovich et al 1997), data taken at PA = 160° and 90°; open green diamonds (Shield & Filippenko 1990), data taken at PA. = 11°.5. Bottom : [OIII]/H β versus [OI]/H α adapted from Ho et al (1997, fig.7 c) : symbols same as in Fig. 6 (bottom).

of 0".1, and extracting fluxes in bins with lengths of 0".2 in the inner 1" and 0".4 farther out.

The line ratios for the GC are different and separated from those of the AGN. They roughly follow the trend of the BB dominated models.

The UV spectra calculated for the the GC regions show many lines with fluxes of $\sim 10^{-4}$ and 10^{-3} erg cm $^{-2}$ s $^{-1}$ for $n_0 \sim 3$ and $n_0 \geq 100$ cm $^{-3}$, respectively (Fig. 2). The star temperature T_* is $\sim 3 \times 10^4$ K and $U \sim 0.01$ (Paper I, Table 2). The HII region models (Contini & Viegas 2001b) with $V_s = 100$ km s $^{-1}$ and $n_0 = 100$ cm $^{-3}$ adopted to reproduce the UV line ratios correspond to lines with absolute fluxes between 10^{-1} and 1 erg cm $^{-2}$ s $^{-1}$ mostly for $T_* = 10^5$ K and $U > 0.1$ (Fig. 8, top).

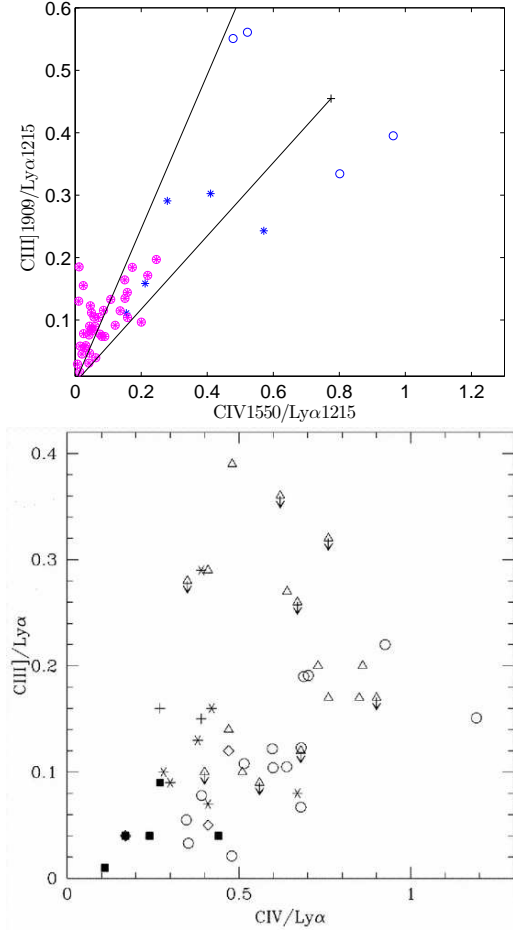


Figure 8. Top: magenta filled circles represent the GC data (Table 1); Contini & Viegas (2001a,b) BB models are represented by black solid lines and pl models by black solid lines connecting black crosses; blue open circles and asterisks from Kraemer et al (2000), SW and NE data, respectively. Bottom : UV spectra from NLS1 (black squares), Seyfert 1 and quasars from Kuraszewicz et al (2000, fig. 1)

3 TURBULENCE, ABUNDANCE FLUCTUATIONS, AND MAGNETIC FIELD

The analysis presented in Paper I invoked the existence of shocks as a necessary ingredient for a consistent derivation of the spectra observed by Simpson et al (2007). Shocks are known to produce turbulence, notably via the Richtmyer-Meshkov instability which is due to the shock acceleration, and is similar to the familiar Raleigh-Taylor instability (see e. g. Mikaelian 1990; Graham & Zhang 2000). Shocks can also lead to other instabilities e.g. shear instability, and Kelvin Helmholtz instability which in turn generate turbulence. Indeed, the clumped and fragmented morphology of the region - that was confirmed in Sect. 2.3 explaining the [OI]6300/H α line ratios - strongly suggests the existence of an underlying supersonic shock-generated turbulence.

Interestingly, a turbulent regime was already predicted by Simpson et al from the characteristic morphological structure of the complex region near the GC.

3.1 Methodology

The existence of turbulence can be probed directly by analyzing the velocity spectrum. In addition, the imprint of turbulence may be detected indirectly by analyzing the power spectrum of "passive scalars" (Lesieur 1997), which are strongly coupled to the gas and follow its turbulent motion (but do not feed-back on the turbulence). The power spectrum of the passive scalar is proportional to the turbulent velocity power spectrum.

Examples are the 21 cm emissivity which is proportional the column density of the neutral hydrogen and its fluctuations reflect those of the density fluctuations and in turn the velocity fluctuations. In the case of infrared continuum it is the dust density, and in the case of abundances ratios it is the density of the specie under consideration.

The observational power spectrum of a passive scalar is a way to measure its hierarchical spatial structure. In cases that it is a power law a hydro-turbulence is naturally suggested as the mechanism that has generated the observed spatial structure. Nevertheless, it is not enough to prove the existence of a hydrodynamical turbulence. On the other hand, if the power spectrum of the velocity field reveals a turbulence, the fact that the power spectra of passive scalars are also power laws with the same slope strengthens the credibility of the deduced velocity turbulence.

An example is the power spectrum of 21cm emission in the small Magellanic cloud (Stanimirovic et al 1999). It was shown by Goldman (2000) that the power spectrum is consistent with that generated by a large scale velocity turbulence. Additional support for the existence of a dynamic turbulence was obtained by Goldman (2007) by deriving the power spectrum of the radial velocities of the giant H_I super-shells of the SMC.

In what follows we analyze the radial velocity data of Simpson et al (2007), and their observed mid-IR continuum flux in order to test for the existence of such a turbulence. Indeed these two kinds of observational data reveal the existence of a supersonic turbulence.

Following these two analyses, we examine the Si/H abundance as function of position *computed* in Paper I. The idea being that if these computations indeed reconstruct the actual physical conditions in the region then the imprint of the turbulence should be evident in the computed abundance as function of position. It turns out to be indeed the case, thus lending credibility to the computations of Contini (2009) as well as to their extensions to the optical and UV ranges presented in previous sections of the present paper.

Finally, we estimate the effect of turbulence on the magnetic field.

3.2 Radial velocities

The 3D spectral function of the turbulent velocity, $\Phi(\vec{k})$ is defined in terms of the 2-point autocorrelation of the turbulent velocity field

$$\Phi(\vec{k}) = \frac{1}{(2\pi)^{3/2}} \int \langle \vec{v}(\vec{r}) \cdot \vec{v}(\vec{r} + \vec{r}') \rangle e^{i\vec{k} \cdot \vec{r}} d^3r$$

In the homogeneous and isotropic case it is useful to introduce the turbulence energy spectrum $E(k)$ and the turbulent velocity spectral function $F(k) = 2E(k)$ so that

$$\Phi(\vec{k}) = \Phi(k) = \frac{F(k)}{4\pi k^2}; k = |\vec{k}|$$

Assuming the ergodic principle, ensemble averages can be replaced by space, surface, or as in the present case line averages.

$$c_r(x) = \langle v_r(x') v_r(x' + x) \rangle = \frac{1}{L} \int_0^L v_r(x') v_r(x' + x) dx'$$

Here, the observed velocity $v_r(x)$ is in effect an intensity-weighted average of the velocity along the line of sight. Under the assumption of homogeneity along the line of sight, the observed velocity is proportional to the integral of the velocity along the line of sight. The resulting value is contributed by all the geometrical depth along the line of sight in the optically thin case or the optically thin part of it.

$F_r(k)$, the power spectrum (the spectral function) of the radial turbulent velocity is the one dimensional Fourier transform of $c_r(x)$

$$F_r(k) = \frac{1}{(2\pi)^{1/2}} \int c_r(x) e^{ikx} dx$$

The power spectrum can also be evaluated by,

$$F_r(k) = |v_r(k)|^2$$

where $v_r(k)$ is the Fourier transform of the velocity

$$v_r(k) = \frac{1}{(2\pi)^{1/2}} \int v_r(x) e^{ikx} dx$$

Since the data are given at a set of discrete positions we compute the power spectrum by the squared absolute value of the discrete Fourier transform of the velocities. This yields the a discrete power spectrum as function of the discrete wavenumber defined as $2\pi/l$, with l being the corresponding spatial scale.

The data are given for 38 positions along an almost straight line with extension of about 75 pc. Not all positions are evenly spaced, thus a numerical uncertainty in the small-scales part of the power spectrum is expected.

Also, the radial velocity observed by Simpson et al (2007) for the m20 position is substantially larger than the adjacent velocities and most likely is due to a local outflow, not typical of the general velocity field. We therefore adopt for this point a value equal to the mean velocity of the other positions.

In Fig. 9 we show the power spectrum of the radial velocities fluctuations, with respect to their mean value. For random residuals the expected power spectrum would have shown no dependence on the wave-number. In contrast, the power spectrum shown in Fig. 9 is a rather steep decreasing function of the relative wavenumber $k = \frac{l_0}{l}$. Here l is the scale corresponding to k , and l_0 is the largest scale corresponds to $k = 1$. The largest scale equals the linear extent of the data strip: about $l_0 = 75$ pc. The value of the root mean square turbulent velocity on the largest scale is $v_0 = 17.4$ km s⁻¹ and exceeds the thermal velocity of ~ 10 km s⁻¹. We believe that the scatter in the points of the power spectrum for the small scales ($k \geq 10; l \leq 7.5$ pc) is an artifact of the uneven spacing, mentioned above.

The line in the figure is a k^{-2} power law that is expected for supersonic turbulence (Passot, Pouquet, & Woodward, 1988; Girimaji & Zhou, 1995). It differs from $k^{-5/3}$ Kolmogorov spectrum which characterizes incompressible turbulence. The steeper slope is due to the fact that a fraction of the turbulent kinetic energy density at a given wavenumber is converted to compression work and decreases the energy transfer to the larger wavenumbers.

Indeed the spectrum derived here is consistent with the k^{-2} spectrum of supersonic turbulence. In order to obtain a quantitative estimate of the goodness of the fit we adopted an uncertainty of 15 km s^{-1} in accord with Simpson et al (2007). Then we generated synthetic velocity data by random generating at each position a velocity using a normal distribution with a mean equal to the observed values and standard deviation of 15 km s^{-1} .

We have built 100 such sets. For each we computed the power spectrum and then computed the standard deviations of the logarithm of the ensuing 100 power spectra. A log-log rather than a linear computation was done as a linear one would completely under-represent the high wave numbers (small spatial scales).

Doing so we obtain a value of $\chi^2 = 0.72$. Some of the uncertainty in the power spectrum is due to the uneven spacing of the positions. The fact that even so the fit is a good one can imply that the true uncertainty in the observed velocities is *smaller* than 15 km s^{-1} .

If one assumes further that the turbulence is isotropic, the value of rms turbulent velocity corresponding to the largest scale would be $\sqrt{3} \times 17.4 = 30 \text{ km s}^{-1}$.

The characteristic timescale of the turbulence is given by $\tau_0 \sim l_0/v_0 \sim 4 \times 10^6 \text{ yr}$. Namely, comparable to the age of the young stellar populations. This is consistent with the framework adopted by Simpson et al (2007) and by Contini (2009) that stellar outflows are the main energy source that shaped the ISM in this region.

Simpson et al (2007) estimate the uncertainty in each radial velocity determination to be $10 - 20 \text{ km s}^{-1}$. Thus, the deduced turbulent velocities from the power spectrum analysis are uncertain by values that are $38^{-1/2}$ smaller namely $\sim 1.6 - 3.2 \text{ km s}^{-1}$. For a relative wavelength of 16 (scale length of about 2.5 pc) the turbulent velocity is 8.7 km s^{-1} larger than the uncertainty by a factor of $\sim 2.7 - 5.4$. Therefore, the derived power spectrum down to these scales can be trusted.

The power spectrum suggests a steepening of the slope to k^{-3} at about $k = 7$. If real, it implies that line of sight depth is about $\frac{1}{7}$ of the extent on the plane of the sky (Goldman 2000); namely a depth of $\sim 10 \text{ pc}$. This is in line with the conclusion of Simpson et al (2007) that there is a non negligible depth to the region.

3.3 Mid-IR flux

The observed flux is an integral of the flux along the line of sight. It is contributed by all the geometrical depth along the line of sight in the optically thin case or the optically thin part of it.

Miville-Deschênes, et al. (2007, 2010) have demonstrated that the fluctuations of the far-IR continuum flux from thermally heated dust in the ISM exhibits a power spectrum identical to that of the velocity turbulence. The

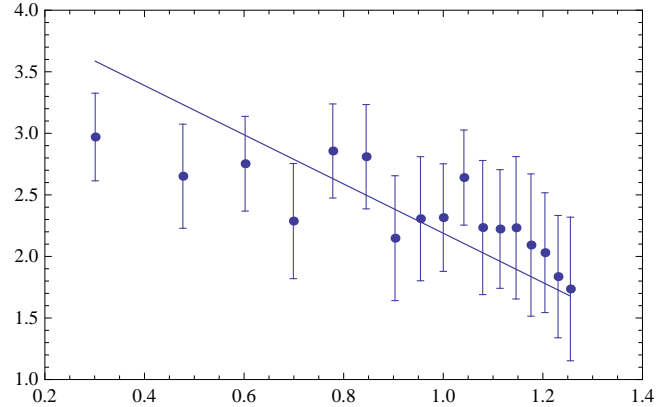


Figure 9. Log of the power spectrum of the radial velocity residuals, in units of $(\text{km s}^{-1})^2$, as function of the log of the relative wavenumber k . $k = 1$ corresponds to the spatial scale $l_0 = 75 \text{ pc}$. The line is a power law with index -2.

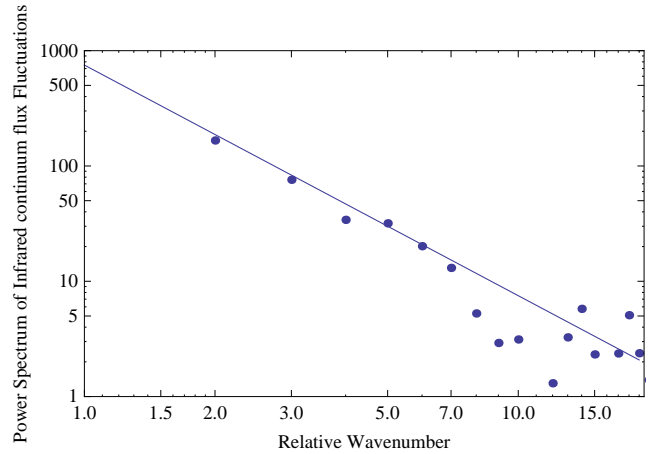


Figure 10. The power spectrum of the fluctuations of the mid-IR continuum at $(13.5 - 14.3) \mu\text{m}$, in units of Jy^2 , as function of the relative wavenumber k . $k = 1$ corresponds to the spatial scale $l_0 = 75 \text{ pc}$. The line is a power law with index -2.

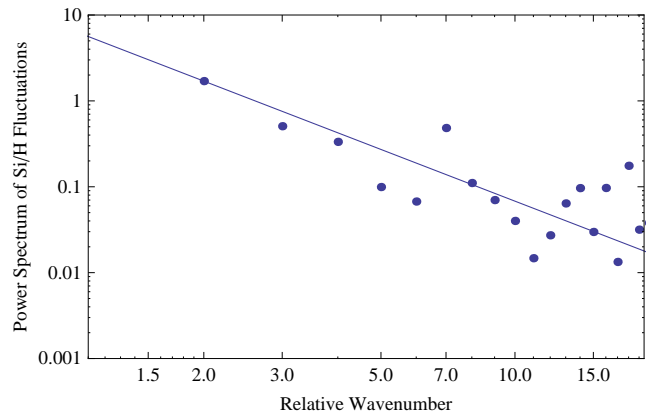


Figure 11. The power spectrum of Si/H fluctuations, in units of 10^{-10} , as function of the relative wavenumber k . $k = 1$ corresponds to the spatial scale $l_0 = 75 \text{ pc}$. The line is a power law with index -2.

interpretation of this result was that the dust is coupled to the gas (Paper I) and thus the dust density fluctuations are determined by the gas turbulence. In the cases considered by these authors the turbulence was subsonic and the power spectrum was the Kolmogorov spectrum.

Here we wish to pursue a similar analysis. But since the turbulence is supersonic we anticipate that also the flux power spectrum would also exhibit the k^{-2} dependence. We use the average continuum flux in the range $(13.5 - 14.3)\mu m$, as function of position, observed by Simpson et al (2007) and derive the power spectrum of the fluctuating flux. We do so by following the same procedure as for the radial velocity with the flux being the quantity whose one-dimensional autocorrelation is being Fourier transformed.

The resulting power spectrum is displayed in Fig. 10. The spectrum exhibits a clear k^{-2} behavior for the larger scales and here too there is an indication of a steepening at about $k = 7$ to a k^{-3} dependence; in effect it is clearer than in the radial velocity spectrum. The uncertainties reported by Simpson et al (2007) are quite small (of the order of 1%). As a result very small uncertainties in the power spectrum are obtained. In this case it is clear that the uncertainties in the power spectrum are dominated by the uneven spacing of the positions.

It is possible to estimate the uncertainties of the uneven spacing by generating synthetic data with randomly spacings (much in the manner we did for the velocity uncertainties as reported above). However this seems to be outside the scope of the present paper. Therefore, we do not derive here a quantitative estimate for the goodness of fit. Rather we would like to draw attention to the fact that the deviations from the power law are at the smaller spatial scales, as expected from uneven spacing, and not on the largest scale. We use this power spectrum as means for lending support to the existence of the supersonic turbulence.

3.4 Si/H abundance

In Paper I the various abundances are computed as function of position. If these computations are a fair representation of the physics in the region, then one expects that the computed values will reflect the turbulence revealed in the observational radial velocity and mid-IR flux.

The abundances can be regarded as a turbulent “passive scalars” (Lesieur 1997). Therefore, the positional fluctuations in the observational abundances can be due to the underlying turbulence. To test this possibility, we chose one of the abundances (Si/H) and computed the power spectrum of the 2 point correlation of its fluctuations, around the mean. We selected Si/H because it does not show drastic variations with position which (as e.g. Fe/H), would imply trapping into dust grains and eventual sputtering.

The computed value is an integral of the abundance along the line of sight. It is contributed by all the geometrical depth along the line of sight in the optically thin case or the optically thin part of it.

The resulting power spectrum is shown in Fig. 11. The power spectrum is consistent with the k^{-2} spectrum of the radial velocity turbulence and that exhibited by the mid-IR flux. This lends credibility to the computational model employed in Paper I and which is used also in the present work. Here, too there is an indication of a steepening of the

spectrum at $k \sim 7$ to a k^{-3} dependence.

In this case too, the deviations of the power spectrum from a power law are manifested mainly on the smaller scales. Here too, the consistency of the power spectrum with what is expected from an underlying supersonic turbulence strengthens the case for the existence of the latter.

3.5 Turbulent Magnetic Field

The high value of the 3-D turbulent velocity can amplify a preexisting magnetic fields up to equilibrium values Shu (1992):

$$\frac{1}{8\pi} B_{turb,eq} = \frac{1}{2} \rho v_{turb}$$

where ρ is the gas density and v_{turb} is the turbulent velocity on the largest scale. For $v_{turb} = 30 \text{ km s}^{-1}$

$$B_{turb,eq} = 140 \mu G (n/100 \text{ cm}^{-3})^{1/2}$$

with n denoting the gas number density. The amplification proceeds via the dynamo mechanism involving the winding up of magnetic field flux lines by the turbulence eddies. Note that on the largest scale the amplification could have been a factor of few because the time available is of the order of turbulence timescale. On smaller scales, the turbulence timescale is shorter and the amplification is larger, but the equilibrium value is smaller.

Fields of this strength and even an order of magnitude higher were reported for the galactic center region (see review by Vallée, 2004). The equilibrium value estimated here refers to the turbulent magnetic field. The larger reported values could evolve from the turbulently amplified field by an inverse cascade process (Mininni 2007) from small to large spatial scales, or directly by shock compression of the magnetic flux lines embedded in the ionized ISM (Medvedev, Silva, & Kamionkowski 2007).

4 CONCLUDING REMARKS

In a previous paper (Paper I) we have calculated the physical and chemical conditions in the nebulae heated and ionized by the star clusters near the GC by detailed modeling the mid-IR line and the continuum spectra observed in 38 positions by Simpson et al. (2007).

Summarizing, in Paper I we found that the spectra near the GC show relatively low ionization due to a low average temperature of the cluster stars (27000-39000 K). The gas pre-shock density and velocity are also low ($\sim 10\text{-}100 \text{ cm}^{-3}$ and $70\text{-}150 \text{ km s}^{-1}$, respectively), the geometrical thickness of the emitting filaments is rather low ($\sim 0.01 \text{ pc}$), and the Fe/H relative abundance is inhomogeneous. In certain positions, e.g. close to the Arched filaments, Fe is trapped into dust grains. The initial magnetic field ranges from 5×10^{-6} to 9×10^{-5} Gauss.

The UV and optical lines cannot be observed due to heavy extinction at these wavelengths. In this paper, spectra were calculated in the UV-optical-IR ranges, using the physical parameters and relative abundances which successfully reproduced the MIR data in Paper I

The line ratios calculated for regions near the GC are

compared with those observed throughout single galaxies, in particular Seyfert 2 galaxies. We have chosen NGC 7130, which contains many starbursts close to the center and in the peripheral zones, and NGC 4151, which has been observed at different positions. The characteristic line ratios in different ranges are also discussed in the light of the diagnostic diagrams assembling large samples of active galaxies.

We have found that the characteristics of the nebulae near the GC are different from those of starburst galaxies and of the NLR of AGN. As a direct consequence of the low density in the nebulae near the GC the line intensities are low compared to active galaxies. Low compression downstream of shock fronts accompanying the low velocity, low density nebulae, lead to the characteristic spectra (Fig. 2), in which e.g. the Ly α line ratios to the strongest UV lines (CIV, CIII] etc) are relatively low compared to those of starburst and AGN ratios (Figs. 3 and 4).

The results show that the geometrical thickness of the emitting filaments is particularly small revealing fragmentation of the emitting matter. The clumped and fragmented morphology of the GC region strongly suggests that it has been shaped by a supersonic turbulence generated by the shocks implied in the modelling (Paper I). Shocks are known to produce turbulence, notably via the Richtmyer-Meshkov instability which is due to the shock acceleration, and is similar to the familiar Raleigh-Taylor instability (see e. g. Mikaelian 1990; Graham & Zhang 2000). Shocks can also lead to other instabilities e.g. shear instability, and Kelvin Helmholtz instability which in turn generate turbulence.

The existence of such a turbulence was confirmed in Sect 3. in the power spectra of the observational radial velocities and mid-IR continuum flux. The turbulence radial rms velocity is about 17 km s⁻¹ and its 3D value is about 30 km s⁻¹. The associated turbulence timescale is about 4 Myr - comparable to the ages of the young stellar populations which are ultimate generators of the shocks and the ensuing turbulence. The turbulence can amplify the initial magnetic fields (Contini 2009) by an order of magnitude.

The power spectra exhibit a k^{-2} behavior typical to supersonic turbulence, and steeper than the Kolmogorov spectrum appropriate for incompressible turbulence. The steepening of the power spectra for relative wave numbers exceeding 7, suggests that the line of sight depth of the turbulent region is about 10 pc.

Interestingly, the Si/H abundance as function of position, *computed* in Paper I, exhibits a power spectrum which is quite similar to the observational power spectra. This lends credibility to computational model employed in Paper I and in the present paper.

ACKNOWLEDGMENTS

We are grateful to the referee for many interesting comments which improved the presentation of the paper. We thank Sharon Sadeh for helpful advise. IG thanks the support from the Afeka College Research Committee.

REFERENCES

- Allen, C.W. 1976 *Astrophysical Quantities*, London: Athlone (3rd edition)
- Atek, H.; Kunth, D.; Hayes, M.; ?stlin, G.; Mas-Hesse, J. M. A&A 2008, 488, 491
- Bertone, S., Schaye, J., Booth, C.M., Dalla Vecchia, C., Theuns, T., Wiersma, R.P.C. 2010, arXiv:1002.3393
- Capak, P. et al 2009, arXiv:0910.0444
- Contini, M. 2009 MNRAS, 399, 1175, Paper I
- Contini, M. 2004 MNRAS, 354, 675
- Contini, M., Viegas, S.M. 2001a, ApJS, 132, 211
- Contini, M., Viegas, S.M. 2001b, ApJS, 137, 75
- Contini, M., Viegas, S. M., Prieto, M. A. 2002 A&A, 386, 399
- Contini, M., Radovich, M., Rafanelli, P., Richter, G.M. 2002, ApJ, 572, 124
- Dudik, R.P., Satyapal, S., Marcu, D. 2009, ApJ, 691, 1501
- Eisenhauer, G. et al. 2005, ApJ, 628, 246 1991, ApJ, 370, L69
- Ghez, A.M. et al. 2005, ApJ, 620, 744
- Girimaji S. S., Zhou Y., 1995, PhLA, 202, 279
- Goldman, I. 2000, ApJ, 54
- Goldman, I. 2007, IAU Symposium 237, 96-1001, 701, arXiv:astro-ph/0703793
- Graham, M. J., Zhang, Q. 2000 ApJS, 127, 339
- Ho, L.C., Filippenko, A.V., Sargent, W.L.W. 1997 ApJS, 112, 315
- Kaufman, M. J., Wolfire, M. G., Hollenbach, D. J., Luhman, M. L. 1999 ApJ, 527, 795
- Kraemer, S. B.; Crenshaw, D. M.; Hutchings, J. B.; Gull, T. R.; Kaiser, M. E.; Nelson, C. H.; Weistrop, D. 2000, ApJ, 531, 278
- Kuraszkiewicz, J. K., Wilkes, B. J., Czerny, B., Mathur, S., Brandt, W. N., Vestergaard, M. 2000 NewAR, 44, 573
- Laursen, P.; Sommer-Larsen, J.; Andersen, A. C. 2009, ApJ, 704, 164
- Maiolino, R. et al. 2005, A&A, 440, L51
- Maiolino, R., Caselli, P., De Zotti, G. 2009 SPICA Workshop.04004. EDP Sciences, 2009
- Medvedev M. V., Silva L. O., Kamionkowski M., 2007, AIPC, 932, 117
- Miville-Deschênes M.-A., Lagache G., Boulanger F., Puget J.-L., 2007, A&A, 469, 595
- Miville-Deschênes M. -, et al., 2010, arXiv, arXiv:1005.2746
- Mikaelian K. O., 1990, PhFl, 2, 592
- Mininni P. D., 2007, PhRvE, 76, 026316
- Molinari, S. et al. 2010, A&A, in press, arXiv:1005.3317
- Nagao, T., Marconi, A., Maiolino, R. 2006 A&A, 447, 157
- Nakanishi, K. & Sofue, Y. 2006, PASJ, 58, 847
- Passot T., Pouquet A., Woodward P., 1988, A&A, 197, 228
- Radovich, M., Rafanelli, P., Birkle, K., Richter, G. 1997, Astron. Nachr., 318, 229
- Rubin, D. et al 2009, A&A, 494, 647
- Schödel, R. Bower, G.C., Muno, M.P., Nayakshin, S., Ott, T. 2006, Journal of Physics: Conference Series, Volume 54, Proceedings of "The Universe Under the Microscope - Astrophysics at High Angular Resolution", held 21-25 April 2008, in Bad Honnef, Germany. Editors: Rainer Schoedel, Andreas Eckart, Susanne Pfalzner and Eduardo Ros, pp. (2006).
- Simpson, J P.; Colgan, S. W. J., Cotera, A. S., Erickson, E.

- F., Hollenbach, D. J., Kaufman, M. J., Rubin, R. H. 2007, ApJ, 670, 1115
- Shields, J. C., & Filippenko, A. V. 1990, AJ, 100, 1034
- Schultheis, M., Sellgren, K., Ramirez, S., Stolovy, S., Ganesh, S., Glass, I. S., Girardi, L. 2009, A&A, 495, 157
- Shu, F. H. 1992. Physics of Astrophysics, Vol. II. University Science Books.
- Spinoglio, L. Malkan, M.A., Smith, H.A., Gonzalez-Alfonso, E., Fischer, J. 200, ApJ, 623, 123
- Stanimirovic S., Staveley-Smith L., Dickey J. M., Sault R. J., Snowden S. L., 1999, MNRAS, 302, 417
- Vallée J. P., 2004, NewAR, 48, 763
- Veilleux, S., Osterbrock, D.E. 1987 ApJ, 63, 295
- Veilleux, S.; Kim, D.-C.; Sanders, D. B., Mazzarella, J. M., Soifer, B. T. 1995 ApJS, 98, 171
- Walter, F. et al. 2009, Nature, 457, 699
- Yusef-Zadeh, F., Morris, M. 1987, ApJ, 320, 557